РОССИЙСКИЙ ГОСУДАРСТВЕННЫЙ ПЕДАГОГИЧЕСКИЙ УНИВЕРСИТЕТ им. А. И. ГЕРЦЕНА
HERZEN STATE PEDAGOGICAL UNIVERSITY of RUSSIA

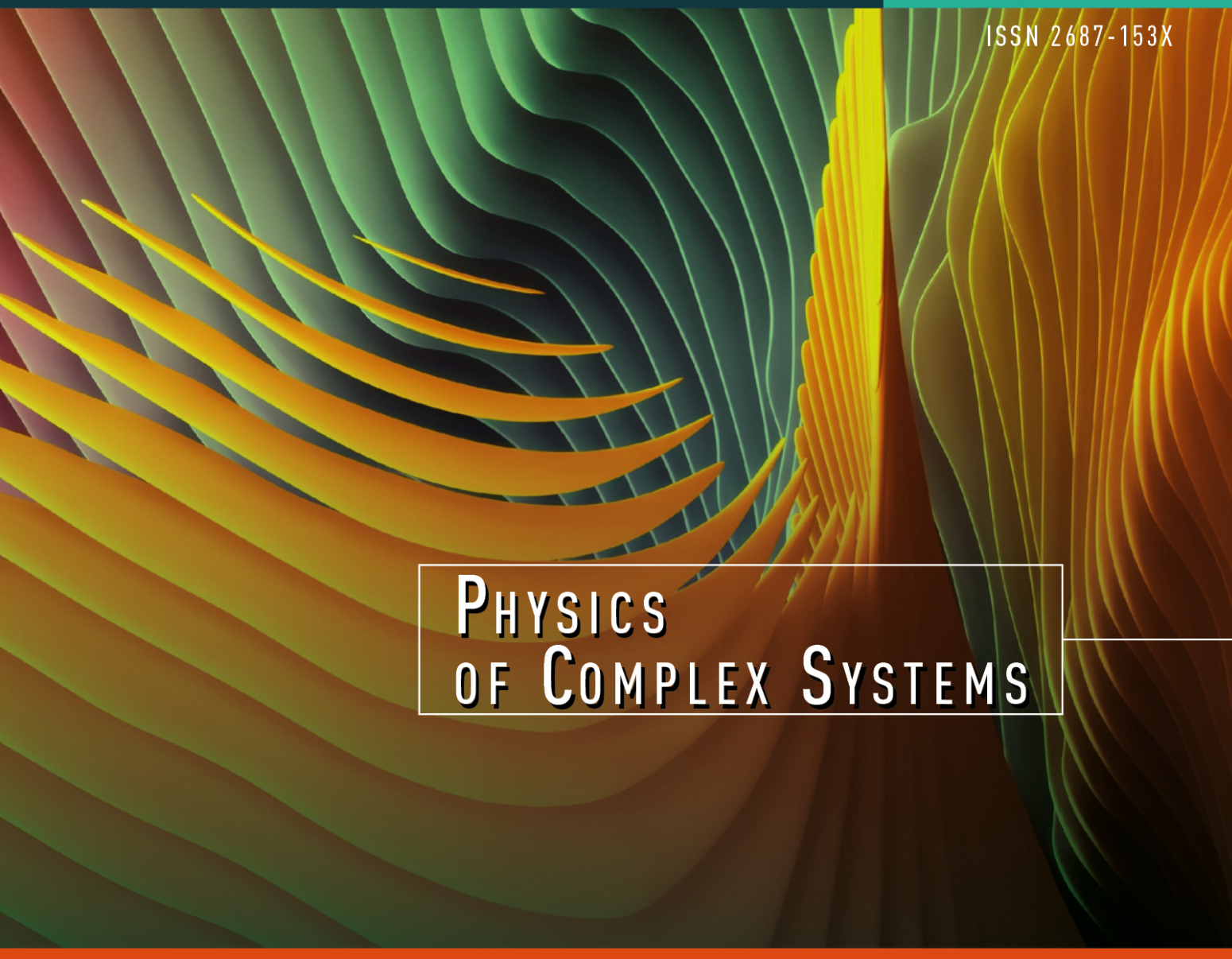

ISSN 2687-153X

Physics of Complex Systems

Т. 2 № 3 2021

Vol. 2 No. 3 2021

Herzen State Pedagogical University of Russia

ISSN 2687-153X (online)
physcomsys.ru
https://www.doi.org/10.33910/2687-153X-2021-2-3
2021. Vol. 2, no. 3

PHYSICS OF COMPLEX SYSTEMS

Mass Media Registration Certificate El No. FS77-77889, issued by Roskomnadzor on 10 February 2020
Peer-reviewed journal
Open Access
Published since 2020
4 issues per year

Publishing house of Herzen State Pedagogical University of Russia
48 Moyka Emb., St Petersburg 191186, Russia
E-mail: izdat@herzen.spb.ru
Phone: +7 (812) 312-17-41

Data size 6,56 Mbyte
Published at 07.09.2021

Editors of the English text *I. A. Nagovitsyna, A. S. Samarsky*
Cover design by *O. V. Rudneva*
Layout by *A. M. Khodan, L. N. Kliuchanskaya*

CONTENTS

Condensed Matter Physics. Dielectric Physics

UDC 538.9

https://www.doi.org/10.33910/2687-153X-2021-2-3-95-100

Dielectric spectroscopy of a composite of polyvinyl alcohol cyanoethyl ether with graphene-modified ferroelectric barium titanates

V. T. Avanesyan✉[1], M. M. Sychev[2], A. G. Chekuryaev[2]

[1] Herzen State Pedagogical University of Russia, 48 Moika Emb., Saint Petersburg 191186, Russia
[2] Saint Petersburg State Institute of Technology, 26 Moscow Ave., Saint Petersburg 190013, Russia

Authors

Vachagan T. Avanesyan, ORCID: 0000-0001-5772-8375, e-mail: avanesyan@mail.ru

Maxim M. Sychev, ORCID: 0000-0001-9736-6452, e-mail: msychov@yahoo.com

Andrew G. Chekuryaev, e-mail: achekuryaev@bk.ru

For citation: Avanesyan, V. T., Sychev, M. M., Chekuryaev, A. G. (2021) Dielectric spectroscopy of a composite of polyvinyl alcohol cyanoethyl ether with graphene-modified ferroelectric barium titanate. *Physics of Complex Systems*, 2 (3), 95–100. https://www.doi.org/10.33910/2687-153X-2021-2-3-95-100

Received 8 May 2021; reviewed 12 June 2021; accepted 12 June 2021.

Funding: The study did not receive any external funding.

Abstract. The paper presents the results of an experimental study of the dielectric properties of a composite with a polymer matrix based on polyvinyl alcohol cyanoethyl ether (CEPVA) with a filler—ferroelectric barium titanate $BaTiO_3$ modified with graphene nanoparticles. The behavior of frequency dependences of the components with complex permittivity and electrical modulus indicates the relaxation character of the dielectric polarization with the participation of polar formations of the functional components of the composite under study.

Keywords: dielectric relaxation, electrical modulus, polymer composite, barium titanate, graphene.

Introduction

Polymer-inorganic composites are widely used in various fields of technology due to the combination of the properties of a polymer and a functional filler. CEPVA stands out among other modern polymeric materials (Avanesyan et al. 2009; 2012). It has the highest dielectric constant (ε) among modern polymers (up to 25) due to the high number of polar nitrile ($C \equiv N$), carbonyl ($C = O$) and hydroxyl (OH) groups. Polymer-inorganic composite materials with a high dielectric constant may find application in protective dielectric layers in capacitors, displays, electroluminescent light sources, and other electronic devices. Creating flexible optoelectronic devices necessitates materials with high dielectric constants, which can be implemented, in particular, by using polymer composites containing CEPVA as a binder with a filler—ferroelectric barium titanate $BaTiO_3$ (Alekseev et al. 2006).

Previously, the possibilities of improving the characteristics of composites were studied by modifying the surface layer of the $BaTiO_3$ filler with Si, Ta, Mg oxides and shungite in order to improve its compatibility with the polymer matrix (Myakin et al. 2011; Sychev et al. 2014). It was found that the modification of the filler allows changing the dielectric constant within wide limits, regulating the interfacial interactions in the system, and also changing the content of active centers on the barium-titanium surface corresponding to the main hydroxyl groups (Bronsted centers) capable of interacting with weakly

acidic hydroxyl groups in CEPVA (Sychev et al. 2016). Creating flexible electronics devices necessitates materials with high dielectric constants, which can be implemented, in particular, by using polymer composites containing polyvinyl alcohol cyanoethyl ether as a binder with a filler—barium titanate modified with graphene (Mjakin et al. 2019).

This article reports the results of an experimental study of the electrophysical properties of a composite based on a CEPVA polymer matrix with a $BaTiO_3$ filler modified with graphene.

Experiment

The samples were layers of a polymer-inorganic composite deposited through a die onto an aluminum foil specially mounted on a glass slide. A CEPVA solution was used as a polymer matrix, in which a barium titanate BaTiO3 powder was dispersed, having a dielectric constant $\varepsilon = 4000$ and a particle size of the order of 1 μm in a ratio of 1.1 ml of polymer solution per 1 g of solution. filler. The thickness of the layers of the obtained composites varied from 20 to 80 μm. The resulting layers were covered with electrodes of conductive glue on silver (contactol). Electrical measurements in the frequency range $5 \cdot 10^2 - 10^5$ Hz were carried out at room temperature using a specially designed measuring cell and LCR-819 precision meter manufactured by GW Instek, Taiwan.

Results and discussion

Fig. 1 shows the frequency dependence of the capacitance of the sample of the composite under study. The values were determined by the standard formula for a flat capacitor. As follows from the data presented, there is a scatter of the real component of the complex dielectric constant $\varepsilon^* = \varepsilon' - i\varepsilon''$ (ε' and ε'' are real and imaginary components of ε^*, respectively), namely, a decrease in its values with an increase in the frequency of the measuring field.

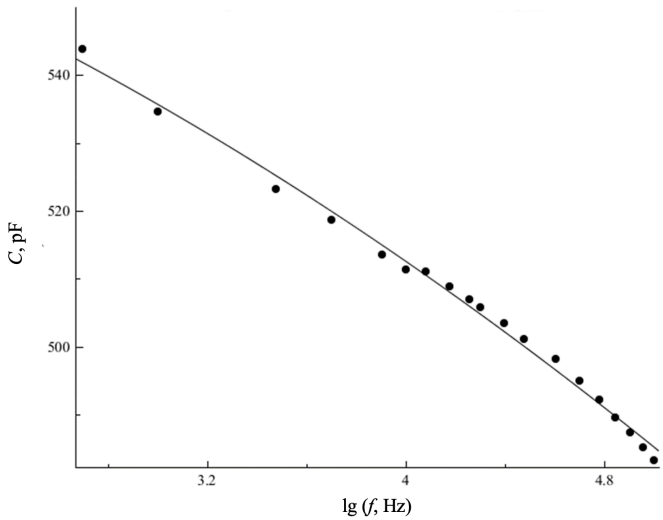

Fig. 1. Frequency dependence of the capacitance of the sample of the CEPVA-modified $BaTiO_3$ composite

The analysis of the available data (Avanesyan et al. 2009; Borodzyulya et al. 2013) shows that the pronounced dispersion of the experimental dielectric characteristics is due to the presence of functional polar groups in the structure of the polymer binder under study (Fig. 2). The relaxing elements in the structure of CEPVA include OH groups, which, according to IR spectroscopy data, refer not only to the binder material, but also to adsorbed water. The OH group is polar due to the difference in the values of the electronegativity of oxygen and hydrogen atoms, and the density of electronic bonds is shifted towards the more electronegative oxygen atom. Two $2sp^3$– atomic orbitals of the CEPVA structure are involved in the formation of bonds of the oxygen atom with the C and H atoms. The oxygen atom contains two lone electron pairs, which are located in the $2s$ and $2p$ positions and stimulate the formation of asymmetric polar coordination. The CN group is also polar due to the different electronegativity of carbon and nitrogen atoms. In this case, the density of electronic bonds shifts towards

 https://www.doi.org/10.33910/2687-153X-2021-2-3-95-100

the more electronegative nitrogen atom. The CN group is distinguished by a pronounced dipole structure, which, due to the presence of a lone electron pair in its structure, can cause the main dielectric response when measured at low frequencies of the electric field.

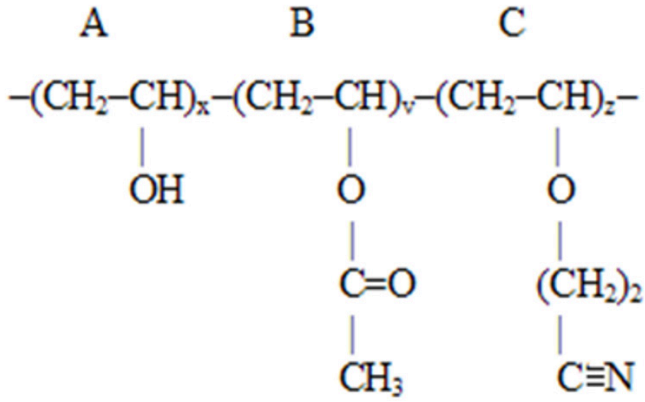

Fig. 2. Structural formula of CEPVA (Borodzyulya et al. 2013)

With increasing frequency, the value of the dielectric loss tangent tan δ of the samples decreases (Fig. 3), reaching a minimum at a frequency of about 10^3 Hz. With a further increase in the field frequency, the values of this parameter increase. It is known that CEPVA films, like films made from other cyano-containing polymers, are characterized by significant through conduction. Thus, the results obtained can also be associated with the integral contribution to the dielectric loss of the processes of conduction and relaxation polarization.

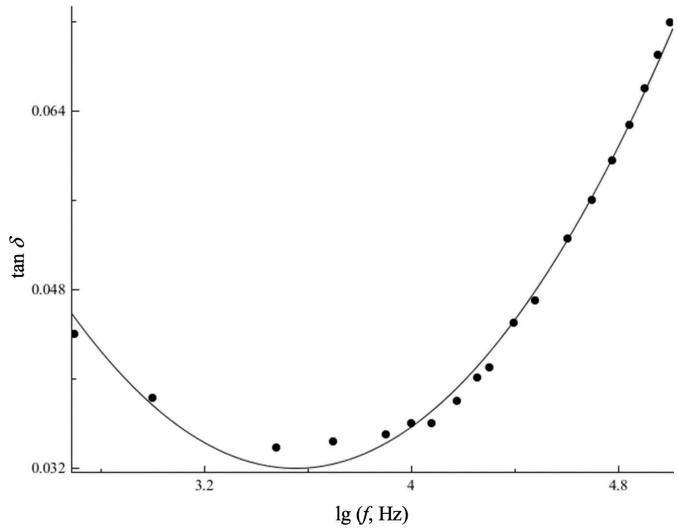

Fig. 3. Frequency dependence of the tan δ of the sample of the CEPVA-modified $BaTiO_3$ composite

The inclusion of graphene nanoparticles leads to a change in the functional composition of the barium titanate surface, associated with a change in the quantitative content of acidic and basic hydroxyl groups, as well as the nature of conjugation of electrons of the lone pair of the hydroxyl group (Sychev et al. 2016). Earlier it was also found (Deb, Ghosh 2010) that the tangent of the dielectric loss angle of the composites under study correlates with the content of surface centers along which water is adsorbed, which determines an increase in this parameter.

In dielectrics, such as, for example, polymer composites, the formation of a space charge can lead to an increase in the local electric field and, as a result, to partial discharges and breakdown. In addition, the accumulation of charge near the electrode causes an abnormally high dielectric constant, which does

not reflect the process of bulk dielectric relaxation, which complicates research in this area. To rationalize the dielectric response of materials with some electrical conductivity, the formalism of the electrical module can be used. This approach makes it possible to interpret the dielectric properties of the sample volume directly with the exclusion of electrode polarization which alleviates the problems caused by electric transport that can mask the dielectric relaxation. The complex electrical modulus M^* is related to the components of the complex dielectric constant and can be represented by the expression (Avanesyan, Salnikova 2017):

$$M^* = \frac{1}{\varepsilon^*} = M' + jM'' = \frac{\varepsilon'}{\varepsilon'^2 + \varepsilon''^2} + j\frac{\varepsilon''}{\varepsilon'^2 + \varepsilon''^2}, \quad (1)$$

where M', M'' are the real and imaginary parts of the complex values of the electrical modulus.

The electrical modulus (M^*) can also be expressed as the Fourier transform of the relaxation function ϕ (t) (Deb, Ghosh 2010):

$$M^* = M_\infty \left[1 - \int_0^\infty \exp(-\omega t) \left(-\frac{d\phi}{dt} \right) dt \right], \quad (2)$$

where the dependence ϕ (t), represented by the so-called Kohlrausch—Williams—Watts function (Williams, Watts 1970), reflects the time process of changing the electric field in the material, described by an extended exponent ϕ (t) = exp [– (t /τ_m)$^\beta$], where τ_m is the conductivity relaxation time, and the value of the exponent β indicates the degree of deviation from relaxation of the Debye type. In turn, the relaxation time associated with the process of electric transport can be found from the graph of the dependence of the component M'' on frequency. The value of the parameter τ_m can also be obtained from its temperature dependence as $\tau_m = \tau_o \exp(E_R / kT)$, where E_R is the activation energy of the relaxation process, τ_o is the preexponential factor, k is the Boltzmann constant, and T is the absolute temperature.

The data of dielectric measurements of the samples of the layers of the investigated composite made it possible to study the behavior of the components of the complex electrical module. At low frequencies, the value of the parameter M' approaches zero (Fig. 4), which indicates the suppression of polarization near the electrode. At high frequencies, the values of M' are characterized by dispersion and reach a maximum value corresponding to $M_\infty = (\varepsilon_\infty)^{-1}$, due to the process of dielectric relaxation, when the displacement frequencies of localized charge carriers and the external electric field coincide. The behavior of the imaginary part of the electrical module reflects the energy loss of the sample in the electric field (Fig. 5). The frequency range below the maximum values of M'' indicates the region in which the drift of ions over long distances is probable. At high frequencies, their mobility decreases, being limited in space by movement only within the boundaries of the corresponding potential wells. The data obtained can vary with a change in the concentration of the modifier, which is due to some changes in the functional composition of the polymer composite.

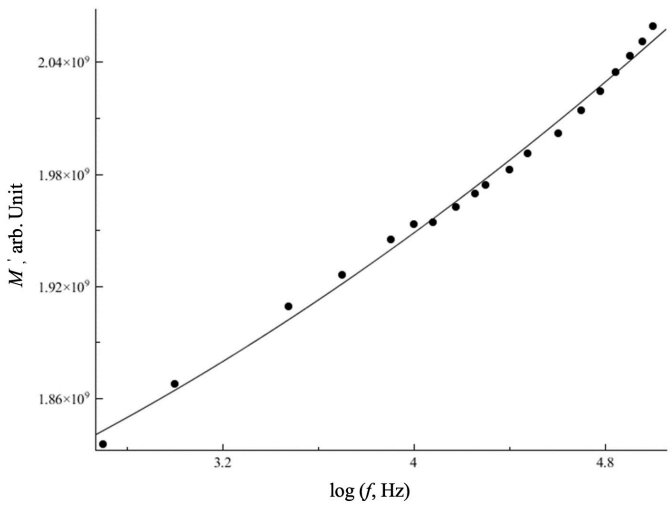

Fig. 4. Frequency dependence of the M' of the sample of the CEPVA-modified $BaTiO_3$ composite

 https://www.doi.org/10.33910/2687-153X-2021-2-3-95-100

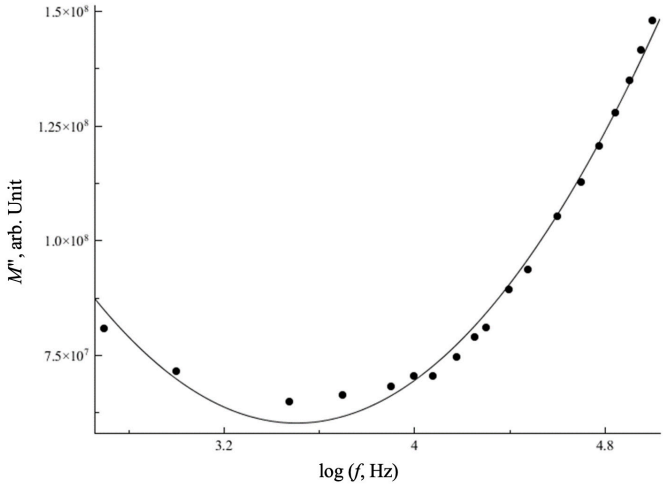

Fig. 5. Frequency dependence of the *M*" of the sample of the CEPVA-modified $BaTiO_3$ composite

Conclusion

Thus, the analysis of the results of dielectric measurements and spectroscopy of the electrical modulus indicates active polarization processes with non-Debye relaxation in the investigated composite. These processes, along with the presence of a filler with a high dielectric constant, are largely associated with the content of polar groups in the CEPVA structure. It can also be noted that the introduction of graphene nanoparticles into the filler of the polymer matrix, i.e., into the ferroelectric $BaTiO_3$, has an additional effect on the dielectric properties of the system under study due to the change in the content of basic and acidic centers of the surface.

Conflict of interest

The authors declare that there is no conflict of interest, either existing or potential.

References

Alekseev, S. A., Korsakov, V. G., Sychev, M. M. et al. (2006) Vliyanie donorno-aktseptornykh tsentrov poverkhnosti titanata bariya na svojstva kompozitov na osnove tsianovogo efira polivinilovogo spirta [Effect of donor-acceptor sites at a barium titanate surface on the properties of composites based on cyanoethyl polyvinyl alcohol]. *Zhurnal fizicheskoj khimii — Russian Journal of Physical Chemistry A*, 80 (4), 700–703. (In Russian)

Avanesyan, V. T., Baranova, E. P., Ogurtsov, K. A., Sychev, M. M. (2012) Dielektricheskaya spektroskopiya funktsional'nogo komponenta tsink-sul'fidnogo elektrolyuminestsentnogo kondensatora [Dielectric spectroscopy of the functional component of a zinc-sulfide electroluminescent capacitor]. *Fundamental'nye problemy radioelektronnogo priborostroeniya*, 12 (1), 96–98. (In Russian)

Avanesyan, V. T., Salnikova, Zh. A. (2017) Formalizm elektricheskogo modulya pri analize dielektricheskikh kharakteristik alifaticheskogo sopoliamida [Formalism of the electrical module in the analysis of dielectric characteristics of aliphatic copolyamide]. *Fundamental'nye problemy radioelektronnogo priborostroeniya*, 17 (2), 362–364. (In Russian)

Avanesyan, V. T., Zagranichek, A. L., Korshunova, M. K. et al. (2009) Elektricheskie svojstva perspektivnogo polimernogo svyazuyushchego dlya elektrolyuminestsentnogo kondensatora [Electrical properties of a promising polymer binder for an electroluminescent capacitor]. *Fundamental'nye problemy radioelektronnogo priborostroeniya*, 9 (1), 223–226. (In Russian)

Borodzyulya, V. F., Myakin, S. V., Sudar', N. T. et al. (2013) Effect of conductivity on the dielectric characteristics of cyano-ethyl ester of poly (vinyl alcohol). *Physics of the Solid State*, 55 (8), 1647–1650. https://doi.org/10.1134/S1063783413080064 (In English)

Deb, B., Ghosh, A. (2010) Dielectric and conductivity relaxation in AgI doped silver selenite superionic glasses. *Journal of Applied Physics*, 108 (7), article 074104. https://doi.org/10.1063/1.3491045 (In English)

Mjakin, S. V., Chekuryaev, A. G., Golubeva, A. I., Sychov, M. M. (2019) Elektricheskie svojstva polimernykh kompozitov na osnove titanata bariya, modifitsirovannogo grafenom [Electric properties of polymer composites

based on barium titanate modified by graphene]. *Izvestiya Sankt-Peterburgskogo gosudarstvennogo tekhnologicheskogo instituta (tekhnicheskogo universiteta) — Bulletin of the Saint Petersburg State Institute of Technology (Technical University)*, 49 (75), 65–68. (In Russian)

Myakin, S. V., Korsakov, V. G., Panova, T. I. et al. (2011) Vliyanie modifitsirovaniya $BaTiO_3$ na dielektricheskuyu pronitsaemost' ego kompozitov s tsianetilovym efirom polivinilovogo spirta [Effect of the modification of barium titanate on the permittivity of its composites with cyanoethyl ester of polyvinyl alcohol]. *Fizika i khimiya stekla*, 37 (6), 61–69. (In Russian)

Sychev, M. M., Minakova, T. S., Slizhov, Yu. G., Shilova, O. A. (2016) *Kislotno-osnovnye harakteristiki poverkhnosti tverdykh tel i upravlenie svojstvami materialov i kompozitov [Acid-base characteristics surfaces of solids and control of properties of materials and composites]*. Saint Petersburg: Khimizdat Publ., 276 p. (In Russian)

Sychev, M. M., Vasina, E. S., Myakin, S. V. et al. (2014) Kompozity tsianetilovogo efira polivinilovogo spirta s $BaTiO_3$, modifitsirovannym shungitovym uglerodom [Composites of polyvinyl alcohol cyanoethyl ether with shungite carbon modified $BaTiO_3$]. *Kondensirovannye sredy i mezhfaznye granitsy — Condensed Matter and Interphases*, 16 (3), 354–360. (In Russian)

Williams, G., Watts, D. C. (1970) Non-symmetrical dielectric relaxation behaviour arising from a simple empirical decay function. *Transactions of the Faraday Society*, 66, 80–85. https://doi.org/10.1039/TF9706600080 (In English)

Condensed Matter Physics. Dielectric Physics

UDC 537.226.4 https://www.doi.org/10.33910/2687-153X-2021-2-3-101-109

Microstructure and properties of polycrystalline PZT films obtained by RF magnetron sputtering with fine variation of the composition near morphotropic phase boundary

D. M. Dolgintsev[1], E. Yu. Kaptelov[2], S. V. Senkevich[2], I. P. Pronin✉[2], V. P. Pronin[1]

[1] Herzen State Pedagogical University of Russia, 48 Moika Emb., Saint Petersburg 191186, Russia
[2] Ioffe Institute, 26 Polytechnicheskaya Str., Saint Petersburg 194021, Russia

Authors
Dmitry M. Dolgintsev, ORCID: 0000-0001-9940-8564, e-mail: nanoherzen@yandex.ru
Evgeny Yu. Kaptelov, ORCID: 0000-0002-7423-6943
Stanislav V. Senkevich, ORCID: 0000-0002-4503-1412
Igor P. Pronin, ORCID: 0000-0003-3749-8706, e-mail: petrovich@mail.ioffe.ru
Vladimir P. Pronin, ORCID: 0000-0001-9335-9781, e-mail: pronin.v.p@yandex.ru

For citation: Dolgintsev, D. M., Kaptelov, E. Yu., Senkevich, S. V., Pronin, I. P., Pronin, V. P. (2021) Microstructure and properties of polycrystalline PZT films obtained by RF magnetron sputtering with fine variation of the composition near morphotropic phase boundary. *Physics of Complex Systems*, 2 (3), 101–109. https://www.doi.org/10.33910/2687-153X-2021-2-3-101-109

Received 24 May 2021; reviewed 7 June 2021; accepted 7 June 2021.

Funding: The study did not receive any external funding.

Abstract. The article discusses the possibilities of fine composition variation of polycrystalline PZT films at the morphotropic phase boundary. The composition of thin films prepared by RF magnetron sputtering of a ceramic target of stoichiometric composition $PbZr_{0.54}Ti_{0.46}O_3$ was varied by changing the distance from the target to the substrate in the range of 30–70 mm. This made it possible to change the composition by ~1.5%. The study focused on the dielectric properties of the formed self-polarized films. The study found that the resistance to external electric fields depends on the conditions of film preparation.

***Keywords*:** method of fine composition variation, PZT, thin films, morphotropic phase boundary, scanning electron microscopy.

Introduction

A popular and highly efficient piezoelectric ceramic based on $PbZr_{1-x}Ti_xO_3$ (PZT) solid solutions was developed in the 1960s. It is still widely used in technical applications. Numerous studies of pre-polarized ceramic PZT samples have shown that high piezoelectric coefficients are observed only in a very narrow range of changes in the Zr/Ti ratio corresponding to the concentration phase transition from the tetragonal to rhombohedral modification of the ferroelectric phase (Fig. 1) (Jaffe et al. 1971).

This region of concentration is usually called the morphotropic phase boundary (MPB). The reasons for the abnormal changes in physical characteristics at the MPB are still a point of controversy, and there are at least several approaches to their explanation (Isupov 1983; Jaffe et al. 1971; Noheda et al. 1999; Sergienko et al. 2002; Wada et al. 2006; Xu 1991). The width of this region is estimated from fractions of a percent to several percent and depends on the ceramic technology, including the temperature and atmosphere of synthesis (and sintering), the presence of excess lead, the purity of the reagents used, grain size, and mechanical stress (Isupov 1983; Jaffe et al. 1971; Xu 1991). In this case, the broadening of the MPB region leads to a decrease in the dielectric and electromechanical parameters.

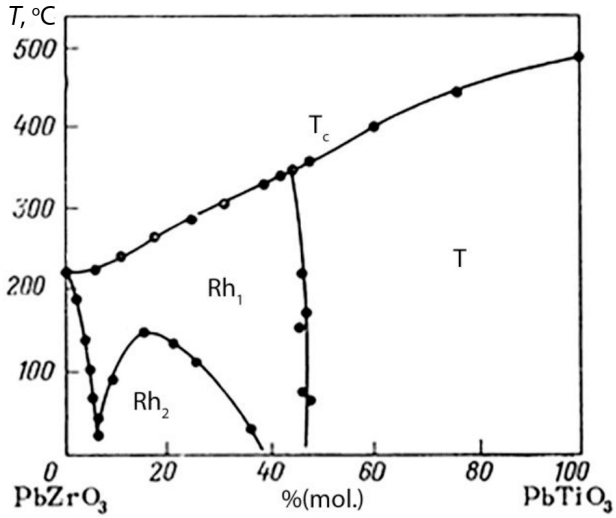

Fig. 1. Phase diagram of ferroelectric $Pb(Zr_{1-x}Ti_x)O_3$ solid solutions. The line separating the T and Rh_1 phases corresponds to the region of the morphotropic phase boundary (Jaffe et al. 1971)

The end of the 20th century witnessed the development of thin-film technologies (both physical and chemical) resulting in rigorous studies of PZT-based thin-film structures. It has been shown that the range of their possible application is much wider than that of ceramics, and covers such areas as non-destructible random-access memory (FRAM) (Izyumskaya et al. 2007; Scott, Paz de Araujo 1989; Scott 1998; Vorotilov et al. 2011), microelectromechanics (MEMS) (Kang et al. 2016; Muralt 2008; Polla 1995; Whatmore 1999), IR technic (Bruchhaus, Pitzer, Schreiter 1999; Whatmore 1999); multiferroics, etc. (Eerenstein et al. 2006; Scott 2007).

For MEMS applications, PZT compositions belonging to MPB are optimal. One of the advantages, is that the produced (virgin) films have macroscopic polarization (self-polarization) and require no additional polarization. In addition, experiments have shown that such films are more resistant to external (electrical, mechanical and thermal) influences (Afanasjev et al. 2001; Bruchhaus et al. 1999; Kholkin et al. 1998; Sviridov et al. 1994).

Finding the compositions with the best properties necessitates fine variation of composition within the MPB range. It is relatively easy to achieve variation with chemical methods of film formation through a simple change in the composition of the precursors. When using physical methods of deposition, for example, the method of magnetron sputtering, a variation may be achieved in the presence of individual targets of metals included in the composition. However, this method is not very reliable for reproducing the composition of the films. When sputtering a ceramic target, changing the composition of the deposited film requires replacing one ceramic target with another.

Nevertheless, in the latter case, it is possible to vary the composition of the films within certain limits by changing the deposition parameters. Thus, it has been shown that by varying the working gas pressure (in the range of 2–60 Pa) during RF magnetron sputtering of a ceramic target of barium-strontium titanate ($Ba_{1-x}Sr_xTiO_3$ or BST), it is possible to change the composition within a fairly wide range (x = 0.3 – 0.65) (Volpyas et al. 2016). The physical reason for this is a change in the length of the thermalization zone. In this case, with an increase in the working gas pressure, the ratio of atoms deposited under directional and diffuse sputtering regimes changes (Volpyas, Kozyrev 2011; Volpyas et al. 2016).

Experiments similar to the studies mentioned above were carried out with RF magnetron sputtering of a ceramic PZT target of composition x = 0.46, where the length of the thermalization zone of the metal atoms of the target also changed. These experiments showed the possibility of changing the composition of the deposited films by ~ 2.5% with a variation in the pressure of the working gas mixture ($Ar + O_2$) in the range of 2–8 Pa (Fig. 2) (Osipov et al. 2018; Pronin et al. 2017). A drawback of the obtained results was the formation of two-phase (perovskite-pyrochlore) films when the working gas pressure dropped below 6 Pa. The reason was the decrease in the lead content in the deposited films below the stoichiometric value.

 https://www.doi.org/10.33910/2687-153X-2021-2-3-101-109

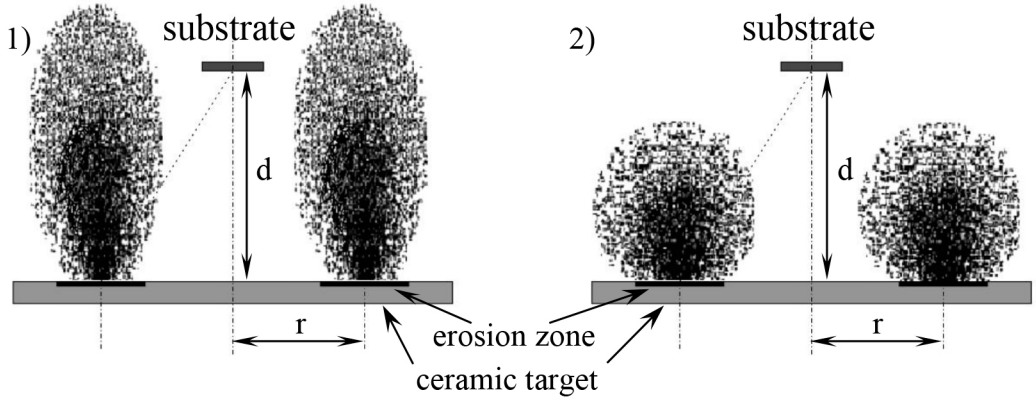

Fig. 2. Sputtering system geometry of the of RF magnetron deposition and the thermalization zone of lead atoms in the working gas plasma at different pressures: 1) 2 Pa; 2) 8 Pa. d = 50 mm, r = 30 mm (Vol'pyas et al. 2019)

The aim of this work was to study the possibility of a fine change in the composition, microstructure, and physical properties of thin films by varying the target-substrate distance ("d") in an RF magnetron sputtering chamber.

Thin film preparation

The films deposition was carried out using divided ceramic PZT target 100 mm in diameter of a stoichiometric composition. The composition of the ceramic target corresponded to the morphotropic phase boundary. The target was sputtered at a gas mixture (80% Ar + 20% O_2) pressure of 8 Pa. At this pressure, the heaviest lead atoms were deposited on the substrate mainly in the diffusion mode. The power supplied to the magnetron (200 W) was kept constant. The distance from the target to the substrate varied in the range of 30–70 mm, while the temperature of the substrate, due to heating in the plasma, varied from 160 to 90 °C. A platinized silicon wafer was used as a substrate. The thickness of the deposited layers was ~500 nm. The deposited films were characterized by an amorphous structure. The mutual geometry of the target and substrate is shown in Fig. 2.

At the second stage of preparation, the samples were annealed in air in a furnace at temperature of T_{ann} = 580 °C (1 hour) to form single-phase perovskite films. To study the electrophysical properties, platinum contact pads with a size of 200 × 200 μm were formed on the surface of the films by the method of RF magnetron sputtering.

Study of composition and microstructure

The composition of thin films was studied using an EVO-40 scanning electron microscope (Carl Zeiss) equipped with an INCA energy dispersive attachment. The incident electron energy was 12 keV, at which the near-surface region of the PZT layer ~300 nm deep was probed.

The composition analysis of the deposited (amorphous) films showed that the elemental ratio of Zr and Ti atoms monotonically changed towards a decrease in the number of titanium atoms with an increase in the target-substrate distance (Fig. 3.1, curve 1). It can be seen from the figure that the range of variation of the composition in the deposited films was ~1.5% from x = 0.485 to x = 0.47. High-temperature annealing led to a change in the elemental ratio of Zr and Ti by ~1.5% (Fig. 3.1, curve 2). The reasons for such changes are not associated with the loss of titanium atoms (the volatility of its oxide vapor is low, in contrast to the anomalously high volatility of lead oxide vapor). Rather, the changes are caused by the segregation of titanium (zirconium) atoms during the crystallization of the perovskite phase. The segregation process is associated with the difference (by more than 100 °C) in the crystallization temperatures of the perovskite phase in lead zirconate and lead titanate (Calame, Muralt 2007). This means that the probability of nucleation of the perovskite phase will be higher in that part of thin layer volume where the local titanium content is higher. The growth of the island is caused by the migration of titanium atoms to the phase boundary of the island and the reverse migration of zirconium atoms.

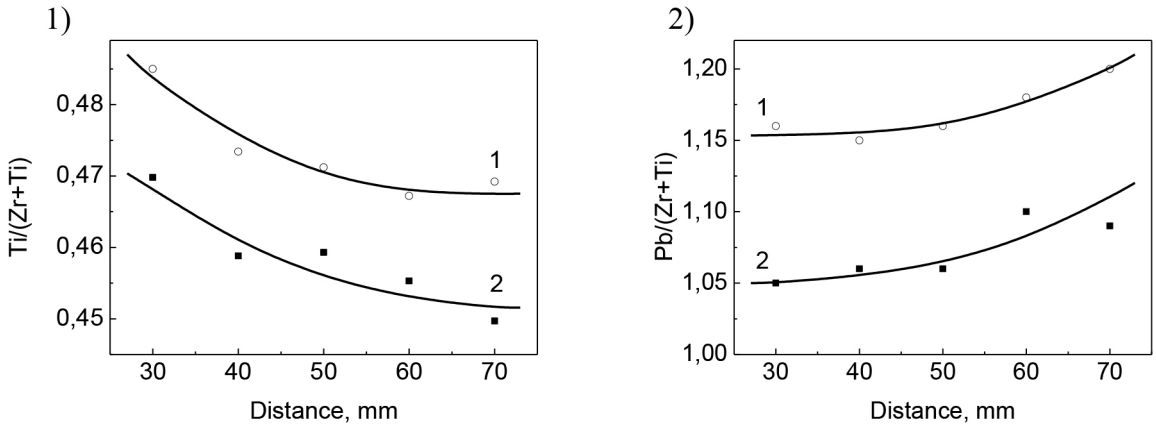

Fig. 3. Changes in the relative content of titanium (1) and lead (2) atoms in PZT films with a change in the target-substrate distance.
The curves correspond to: 1—amorphous phase, 2—perovskite phase. Annealing temperature—580 °C

The location of the predominant nucleation (and growth) of perovskite islands over the polycrystalline layer thickness (near interfaces or in the bulk of the layer, Fig. 4) is determined by a number of competing factors. These include the local presence of lead excess, the presence of sublayers that facilitate the nucleation of the perovskite phase, and the difference in mechanical conditions at the upper and lower interfaces and in the bulk of the thin film. For the predominant nucleation of the perovskite phase near the lower interface (near the boundary of the PZT layer and the lower platinum electrode), nanolayers of titanium dioxide or metallic titanium are often used, previously deposited on the surface of the lower electrode. These nanolayers also determine the orientation of the growth texture of a thin film with a predominant "100" or "111" orientation (Pronin et al. 2013; Willems et al. 1997). In the absence of such nanolayers, the minimization of the formation energy of perovskite islands will be determined by the presence of excess lead.

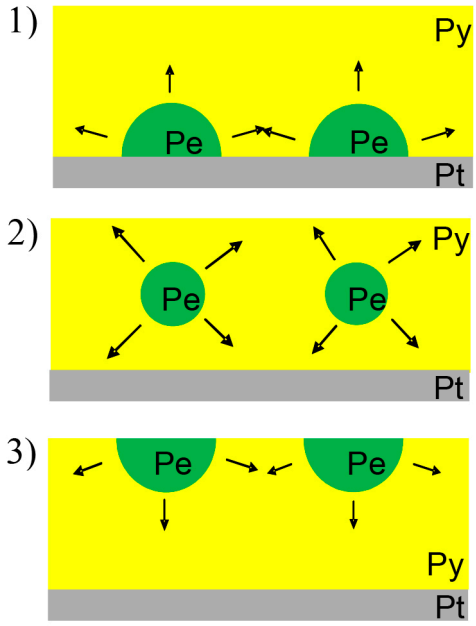

Fig. 4. Schematic models of the perovskite (Pe) phase nucleation in the matrix of the pyrochlore (Py) phase: near the lower interface (1), in the bulk (2) and near the upper interface of the PZT layer (3).
The arrows show the direction of Pe islands growth

https://www.doi.org/10.33910/2687-153X-2021-2-3-101-109

In our case, in the presence of a predominant <110> growth texture of the formed films (Pronin et al. 2010), a decrease in the titanium content in the upper part of the film indicates that the nucleation and growth of perovskite islands occurs mainly near the lower PZT layer interface. Judging by the monotonic change in the Zr/Ti ratio, this mechanism works during the formation of the perovskite phase in all the films under study, i.e., for all values of "d".

Fig. 3.2 shows the change in the lead content with a variation in the target-substrate distance in amorphous and annealed films. An increase in the lead content in amorphous films (curve 1) with an increase in "d", as noted earlier, is associated with a change in the thermalization zone length of the heaviest atoms (lead) (Fig. 2). The relatively low excess of lead over the stoichiometric content and its loss during annealing also indicates that the nucleation of islands of the perovskite phase and their growth occurs in the lower part of the thin layer, or in its bulk, Fig. 4.1 and 4.2. In this case, there will be a directed migration of titanium atoms from the surface into the depth of the film, and zirconium atoms in the opposite direction.

Thus, on the one hand, by varying the target-substrate distance, it was possible to finely vary the integral composition of the deposited films within 1.5%, but on the other hand, all the films formed were also characterized by a gradient distribution of Zr (Ti) atoms over the thickness. From Fig. 3.1 it follows that the value of the gradient is close to 1.5%. It should be noted that this result is not optimal when it comes to achieving the highest dielectric and electromechanical parameters due to the "diffuseness" of the MPB.

The microstructure of the near-surface layer of perovskite films was studied in the back scattering electron mode at the incident electron energy of 12 keV. The microstructure was a set of polycrystalline blocks ~20–40 μm in size (Fig. 5). The internal structure of the blocks consisted of separate rays emanating from a single center. The highest density of rays was observed in films deposited at "d" = 30 mm (Fig. 5.1), the minimum at "d" = 70 mm (Fig. 5.5), where the boundaries of the rays lost their clear outlines, and their number sharply decreased. The reasons for these changes are still unclear as well as the reasons for the emergence of a spherulite radiant structure. The study of the nature of spherulites observed during the crystallization of various types of compounds requires additional investigations.

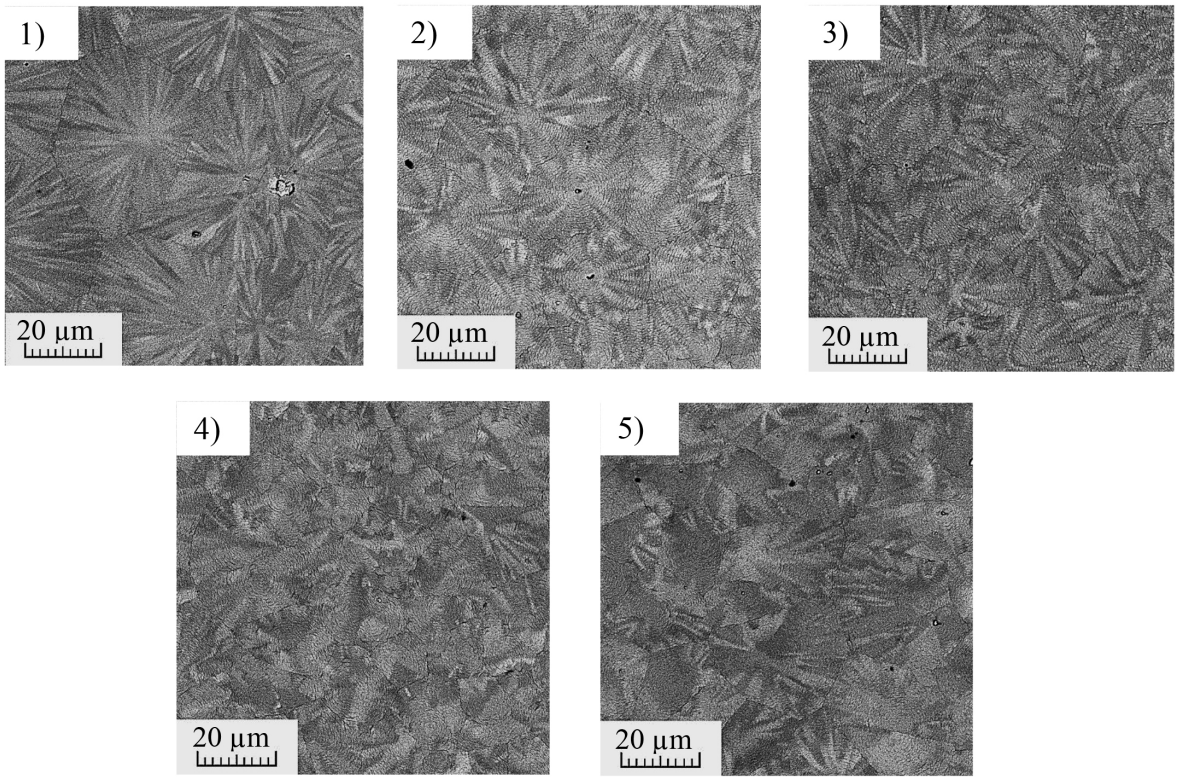

Fig. 5. SEM images of the spherulite microstructure of the perovskite thin PZT films deposited at different target-substrate distances (d): 1)—30 mm; 2)—40 mm; 3)—50 mm; 4)—60 mm; 5)—70 mm

Dielectric properties study

Fig. 6 shows the dependence of the dielectric constant (ε_k) of the samples on the target-substrate distance measured at a frequency of 10 kHz using an E7-20 immittance meter. The dependence is a curve with a minimum. This behavior can be associated with the simultaneous influence of a number of factors, such as a possible difference in the crystallization temperature of the perovskite phase and the redistribution of excess lead in the film volume, a decrease in the substrate temperature caused by plasma heating with increasing "d".

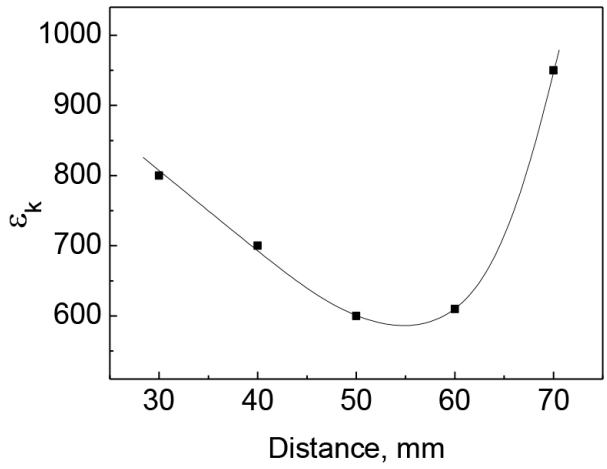

Fig. 6. Experimental dependence of the effective dielectric constant (ε_k) of PZT films on target-substrate distance. The measurement frequency—10 kHz

The value of the internal field (E_{int}), by which one can qualitatively judge the self-polarization of thin films (in the first approximation, these parameters change proportionally), changed rather strongly with a change in the distance from the target to the substrate. This value is usually determined from the shift of the capacitance-voltage characteristics (reverse dependences of the dielectric constant) (Fig. 7), or from the shift of the dielectric hysteresis loops along the abscissa axis (Fig. 8). In the latter case, due to the high frequency of the electrical impact, the definition of E_{int} turns out to be more accurate.

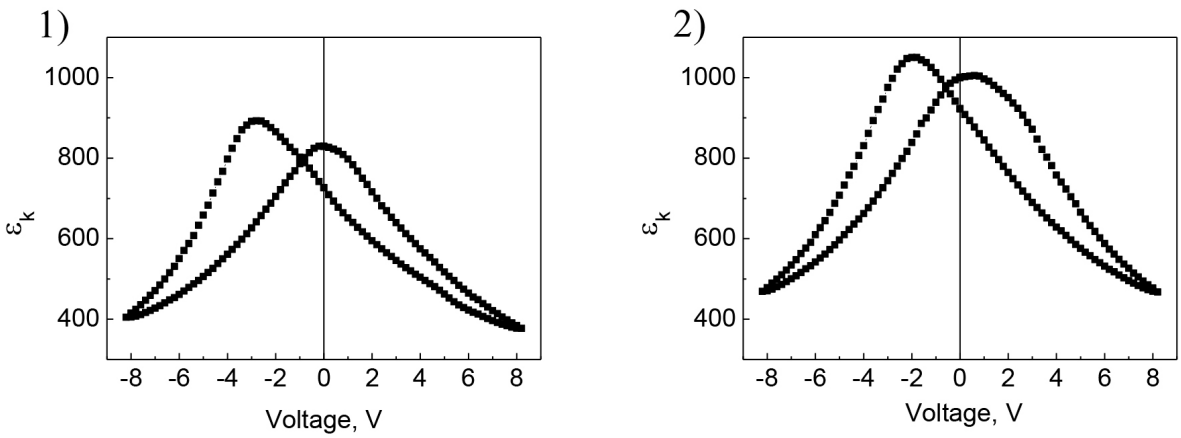

Fig. 7. Reversible dependences (ε-V) of perovskite PZT films deposited at d = 30 mm (1) and d = 70 mm (2). Measurement frequency—10 kHz

 https://www.doi.org/10.33910/2687-153X-2021-2-3-101-109

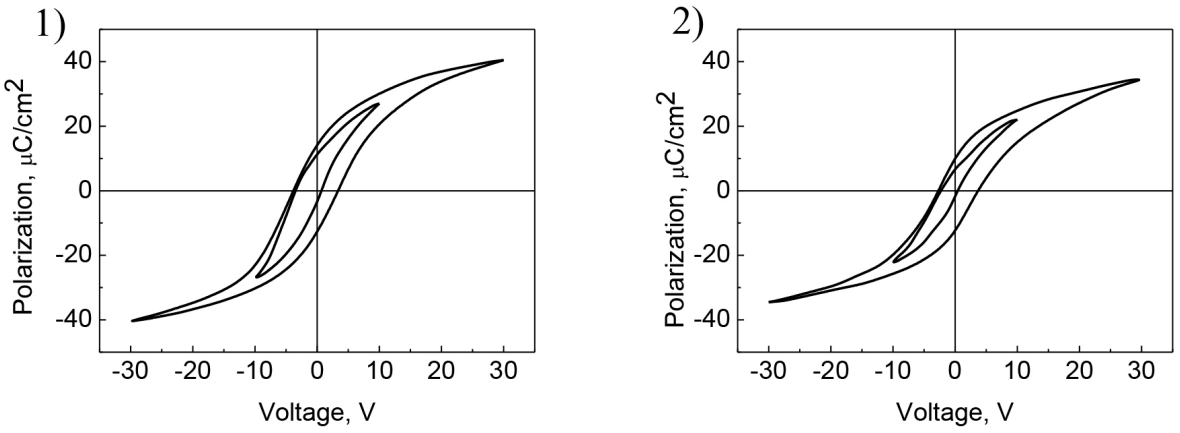

Fig. 8. Dielectric hysteresis loops of perovskite PZT films deposited at different target-substrate distances: 30 mm (1) and 70 mm (2)

Fig. 9 shows the values of the internal field determined from the dielectric hysteresis loops at different amplitudes of the applied alternating field. Films deposited at "d" = 30 mm were characterized by high values of the internal field, reaching E_{int} ~25 kV/cm, in an alternating field of ~200 kV/cm (curve 1), and at "d" = 70 mm it decreased almost twice (Fig. 9, curve 3). In strong fields, ~400 kV/cm, the stability of the internal field to external influences remained high for films deposited at "d" = 30 mm, while at high values of "d" the dielectric hysteresis loops became almost symmetric (Fig. 8.2). The reason for the high stability of the internal field (self-polarization) is apparently associated not only with a high concentration of excess lead oxide localized near the lower interface of the film, but also with a change in its location (Osipov et al. 2015).

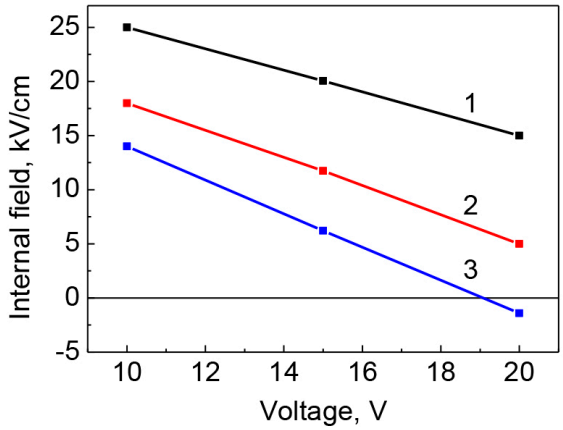

Fig. 9. Experimental dependences of the internal field values (E_{int}) determined from dielectric hysteresis loops (frequency—1 kHz) depending on the applied alternating voltage in PZT films deposited at d = 30 mm (1), d = 50 mm (2) and d = 70 mm (3)

Conclusions

Thus, as a result of studying the films prepared by varying the substrate — target distance in the range of 30–70 mm in the chamber of RF magnetron sputtering of a ceramic target, it was revealed that:

1) the composition of the deposited (amorphous) films varied in the range of 1.5%. This compositional change covers a significant area of MPB. Subsequent annealing led to a small gradient of Zr (Ti)

atoms, leading to "smearing" of MPB and, as a consequence, to deterioration of the physical characteristics;
2) annealing of the deposited films at 580 °C led to the formation of a single-phase perovskite structure;
3) the nature of the spherulite (perovskite) microstructure changed significantly;
4) the stability of the self-polarized state, determined by the magnitude of the internal field, strongly depended on the target-substrate distance, which can be associated both with the redistribution of excess lead over the thickness of the films and with a change in the appearance of the radiant spherulite structure.

Conflict of Interest

The authors declare that there is no conflict of interest, either existing or potential.

References

Afanasjev, V. P., Petrov, A. A., Pronin, I. P. et al. (2001) Polarization and self-polarization in thin $PbZr_{1-x}Ti_xO_3$ (PZT) films. *Journal of Physics Condensed Matter*, 13 (39), article 8755. https://www.doi.org/10.1088/0953-8984/13/39/304 (In English)

Bruchhaus, R., Pitzer, D., Schreiter, M., Wersing, W. (1999) Optimized PZT thin films for pyroelectric IR detector arrays. *Journal of Electroceramics*, 3 (2), 151–162. https://doi.org/10.1023/A:1009995126986 (In English)

Calame, F., Muralt, P. (2007) Growth and properties of gradient free sol-gel lead zirconate titanate thin films. *Applied Physics Letters*, 90 (6), article 062907. https://doi.org/10.1063/1.2472529 (In English)

Eerenstein, W., Mathur, N. D., Scott, J. F. (2006) Multiferroic and magnetoelectric materials. *Nature*, 442 (7104), 759–765. https://doi.org/10.1038/nature05023 (In English)

Isupov, V. A. (1983) Some aspects of the physics of piezoelectric ceramics. *Ferroelectrics*, 46 (1), 217–225. https://doi.org/10.1080/00150198308225269 (In English)

Izyumskaya, N., Alivov, Y.-I., Cho, S.-J. et al. (2007) Processing, structure, properties, and applications of PZT thin films. *Critical Reviews in Solid State and Materials Sciences*, 32 (3-4), 111–202. https://doi.org/10.1080/10408430701707347 (In English)

Jaffe, B., Cook, W., Jaffe, H. (1971) *Piezoelectric ceramics*. London; New York: Academic Press, 328 p. (In English)

Kang, M.-G., Jung, W.-S., Kang, Ch.-Y., Yoon, S.-J. (2016) Recent progress on PZT based piezoelectric energy harvesting technologies. *Actuators*, 5 (1), article 5. https://doi.org/10.3390/act5010005 (In English)

Kholkin, A. L., Brooks, K. G., Taylor, D. V. et al. (1998) Self-polarization effect in $Pb(Zr,Ti)O_3$ thin films. *Integrated Ferroelectrics*, 22 (1-4), 525–533. https://doi.org/10.1080/10584589808208071 (In English)

Muralt, P. (2008) Recent progress in materials issues for piezoelectric MEMS. *Journal of the American Ceramic Society*, 91 (5), 1385–1396. https://doi.org/10.1111/j.1551-2916.2008.02421.x (In English)

Noheda, B., Cox, D. E., Shirane, G. (1999) A monoclinic ferroelectric phase in the $Pb(Zr_{1-x}Ti_x)O_3$ solid solution. *Applied Physics Letters*, 74 (14), article 2059. https://doi.org/10.1063/1.123756 (In English)

Osipov, V. V., Kiselev, D. A., Kaptelov, E. Yu. et al. (2015) Internal field and self-polarization in lead zirconate titanate thin films. *Physics of the Solid State*, 57 (9), 1793–1799. http://dx.doi.org/10.1134/S1063783415090267 (In English)

Osipov, V. V., Kaptelov, E. Yu., Senkevich, S. V. et al. (2018) The study of self-poled PZT thin films under variation of lead excess. *Ferroelectrics*, 525 (1), 76–82. https://doi.org/10.1080/00150193.2018.1432931 (In English)

Polla, D. L. (1995) Microelectromechanical systems based on ferroelectric thin films. *Microelectronic Engineering*, 29 (1-4), 51–58. https://doi.org/10.1016/0167-9317(95)00114-X (In English)

Pronin, I. P., Kaptelov, E. Yu., Senkevich, S. V. et al. (2010) Crystallization of thin polycrystalline PZT films on Si/SiO_2/Pt substrates. *Physics of the Solid State*, 52 (1), 132–136. https://doi.org/10.1134/S1063783410010233 (In English)

Pronin, I. P., Kaptelov, E. Yu., Senkevich, S. V. et al. (2013) Vliyanie mezhfaznykh granits i nanovklyuchenij oksida svintsa na strukturnye i segnetoelektricheskie svojstva tonkikh plenok PZT [Influence of interphase boundaries and nanoinclusions of lead oxide on the structure and ferroelectric properties of PZT thin films]. *Nanomaterialy i nanostruktury — XXI vek — Nanomaterials and Nanostructures XXI-Century*, 4 (4), 21–29. (In Russian)

Pronin, I. P., Kukushkin, S. A., Spirin, V. V. et al. (2017) Formation mechanisms and the orientation of self-polarization in PZT polycrystalline thin films. *Materials Physics and Mechanics*, 30 (1), 20–34. (In English)

Scott, J. F. (1998) The physics of ferroelectric ceramic thin films for memory applications. *Ferroelectrics Review*, 1 (26), 1–129. (In English)

Scott, J. F. (2007) Application of modern ferroelectrics. *Science*, 315 (5814), 954–959. https://doi.org/10.1126/science.1129564 (In English)

Scott, J. F., Paz de Araujo, C. A. (1989) Ferroelectric memories. *Science*, 246 (4936), 1400–1405. https://doi.org/10.1126/science.246.4936.1400 (In English)

Sergienko, I. A., Gufan, Yu. M., Urazhdin, S. (2002) Phenomenological theory of phase transitions in highly piezoelectric perovskites. *Physical Review B*, 65 (14), article 144104. https://doi.org/10.1103/PhysRevB.65.144104 (In English)

Sviridov, E., Sem, I., Alyoshin, V. et al. (1994) Ferroelectric film self-polarization. *MRS Online Proceedings Library*, 361 (1), 141–146. https://doi.org/10.1557/PROC-361-141 (In English)

Volpyas, V. A., Tumarkin, A. V., Mikhailov, A. K. et al. (2016) Ion plasma deposition of oxide films with graded-stoichiometry composition: Experiment and simulation. *Technical Physics Letters*, 42 (7), 758–760. https://doi.org/10.1134/S1063785016070300 (In English)

Volpyas, V. A., Kozyrev, A. B. (2011) Thermalization of atomic particles in gases. *Journal of Experimental and Theoretical Physics*, 113 (1), article 172. https://doi.org/10.1134/S1063776111060227 (In English)

Vorotilov, K. A., Mukhortov, V. M., Sigov, A. S. (2011) *Integrirovannye segnetoelektricheskie ustrojstva [Integrated ferroelectric devices]*. Moscow: Energoatomizdat Publ., 175 p. (In Russian).

Vol'pyas, V. A., Kozyrev, A. B., Tumarkin, A. V. et al. (2019) The element composition variation in lead zirconate titanate upon the ion-plasma deposition: Experiment and simulation. *Physics of the Solid State*, 61 (7), 1223–1227. https://doi.org/10.1134/S1063783419070308 (In English)

Wada, S., Yako, K., Yokoo, K. et al. (2006) Domain wall engineering in barium titanate single crystals for enhanced piezoelectric properties. *Ferroelectrics*, 334 (1), 17–27. https://doi.org/10.1080/00150190600689647 (In English)

Whatmore, R. W. (1999) Ferroelectrics, microsystems and nanotechnology. *Ferroelectrics*, 225 (1), 179–192. https://doi.org/10.1080/00150199908009126 (In English)

Willems, G. J., Wouters, D. J., Maes, H. E., Nouwen, R. (1997) Nucleation and orientation of sol-gel PZT films on Pt electrodes. *Integrated Ferroelectrics*, 15 (1-4), 19–28. https://doi.org/10.1080/10584589708015693 (In English)

Xu, Y. (1991) *Ferroelectric materials and their applications*. Amsterdam: North Holland Publ., 391 p. (In English)

Condensed Matter Physics.
Physics of Low-Dimensional Structures and Nanostructures

UDC 538.9+535.3 https://www.doi.org/10.33910/2687-153X-2021-2-3-110-114

Additional dye options for spectral sensitization of photo processes in silver stearate—silver bromide system

M. A. Goryaev✉[1], A. P. Smirnov[1], A. A. Luzhkov[1]

[1] Herzen State Pedagogical University of Russia, 48 Moika Emb., Saint Petersburg 191186, Russia

Authors

Mikhail A. Goryaev, ORCID: 0000-0002-2182-6763, e-mail: mgoryaev@mail.ru

Alexander P. Smirnov, ORCID: 0000-0003-2463-2056, e-mail: Smirnov_Alexander_hspu@mail.ru

Alexander A. Luzhkov, ORCID: 0000-0003-4392-0838, e-mail: Yandexbox@mail.ru

For citation: Goryaev, M. A., Smirnov, A. P., Luzhkov, A. A. (2021) Additional dye options for spectral sensitization of photo processes in silver stearate—silver bromide' system. *Physics of Complex Systems*, 2 (3), 110–114. https://www.doi.org/10.33910/2687-153X-2021-2-3-110-114

Received 31 March 2021; reviewed 19 May 2021; accepted 20 May 2021.

Funding: This research has no any financial support.

Abstract. The paper discusses spectral sensitized photo processes in silver bromide caused by dyes adsorbed on the surface of silver stearate via the lightguide mechanism and a direct hit of the luminescent light from dye molecules localized near the microcrystal of silver bromide to the microcrystal of silver bromide. The paper submits an estimation of the contribution of dye molecules localized on the surface of silver stearate to overall spectral sensitization. These calculations demonstrate that the contribution of dye molecules adsorbed on the particle of silver stearate to spectral sensitization of silver stearate—silver bromide structure is comparable to the contribution of dye molecules placed on the microcrystal of silver bromide. Dye molecules localized on the particle of silver stearate allow to raise the efficiency of spectral sensitization by 40 to 60 percent.

Keywords: spectral sensitization, thermally developable photographic materials, silver stearate–silver bromide structure, lightguide mechanism, luminescence of adsorbed dyes, computer calculations.

Introduction

Organic dyes are effective in spectral sensitization of photophysical and photochemical processes in different semiconductors (AgHal, ZnO, TiO_2 and other) both in visible and infrared ranges (Akimov et al. 1980; Goryaev 2015; 2016; 2018; 2019; James 1977). Spectral sensitization is the most effective control method of the sensitivity degree and the sensitivity spectrum for classic silver halide photo materials (James 1977). The photoelectrochemical cells based on TiO_2 particles with adsorbed sensitizing dyes are an alternative to silicon solar cells (Gratzel 2003). The photothermographic materials based on silver halide and silver salts of fatty acids (in particular, silver stearate) are used widely in the recording of optical images (Goryaev 1991; Morgan 1993; Sahyun 1998). When preparing such photosensitive composition, silver bromide is synthesized on the surface of silver stearate (Goryaev et al. 1992; Goryaev 1994a). The addition of organic sensitizing dyes to the compositions provides spectral sensitization of these photo materials in visible and infrared range (Goryaev et al. 1992; Goryaev, Shapiro 1997). The optimal concentration of sensitizing dyes for photothermographic materials is about one hundred times more than the optimal concentration of these dyes for classic silver halide photo materials (Goryaev et al. 1992). Dye molecules precipitate both on the surface of silver stearate and on the surface of silver bromide when this dye is adsorbed into photothermographic compositions. The paper explores spectral sensitized photo processes in silver bromide caused by dyes adsorbed on the surface of silver stearate.

The paper also submits an estimation of the contribution of dye molecules localized on silver stearate surface to the overall spectral sensitization.

Results and discussion

The scanning electron microscopy of photo thermo structures has indicated that cube microcrystals of silver bromide of around 0.1 μm form on the surface of silver stearate at the optimal concentration of silver bromide to silver stearate of 10 mol% (Goryaev 1994a; Goryaev, Smirnov 2020a). The particles of silver stearate are oblong prisms about 1 μm in length and the height of 3 to 5 times smaller than the length. In this case, the relation of silver stearate surface area to silver bromide surface area is 30 to 50. As a first approximation, the quantity of dye molecules localized on the surface of silver stearate is also 30 to 50 times bigger than the quantity of dye molecules placed on the microcrystal of silver bromide. This fact explains the difference of optimal concentrations of dyes for classic silver halide materials and photothermographic materials.

The transfer of energy from dye molecules localized on the surface of silver stearate into the microcrystal of silver bromide via an inductive resonant mechanism (Ermolaev et al. 1996) cannot be significant at this particle sizes because critical radius of such transfer is 6 to 8 nm (Akimov et al. 1980). Besides, the electrons from the excited dye molecules cannot pass through the silver stearate layer because silver stearate is a typical dielectric. Dye molecules adsorbed on non-light sensitive silver stearate radiate with luminescence quantum yield of a few dozen percent (Goryaev, Smirnov 2020a; 2020b). Silver stearate is a transparent dielectric in the visible range which makes it possible for dye luminescent light to hit into the microcrystal of silver bromide through the silver stearate particle. The absorption and luminescence spectra of the dyes adsorbed on silver stearate strongly overlap. This fact stipulates the effective absorption of the luminescent light by dye molecules localized on the microcrystal of silver bromide. Consequently, spectral sensitization effectiveness of photo processes in silver halide increases according to the classic theories of spectral sensitization process (Akimov et al. 1980).

The lightguide mechanism in silver stearate—polyvinylbutyral system (polyvinylbutyral is a binder component in photothermographic materials), the strong overlapping of dye luminescence and absorption spectra, the significant quantum luminescence yield of different dyes adsorbed on the surface of silver stearate are indicative of the significant contribution of dye molecules placed on the particle of silver stearate in spectral sensitization of photothermographic materials.

In complex photothermographic structures the silver stearate—silver bromide system locates in the binder component—polyvinylbutyral. The total internal reflection on the optical interface of silver stearate—polyvinylbutyral is provided by the lightguide mechanism of spectral sensitization (Goryaev 1994b; 1998). The refractive index of polyvinylbutyral is 1.485 (Kabanov 1974). In turn, the refractive index of silver stearate is 1.515 (Goryaev, Smirnov 2012). As a result, the luminescent light in silver stearate realizes total internal reflection at angles of incidence of about 78.5°. This value allows to conclude that the lightguide mechanism of spectral sensitization in photothermographic materials is effective enough.

The contribution of dye molecules adsorbed on the particle of silver stearate to spectral sensitization was calculated according the model shown in Figure 1*a*. The silver stearate particle sizes are 1000 × 500 × 500 nm. The silver bromide microcrystal sizes are 100 × 100 × 100 nm. The dye molecule size is 5 nm. The distance between dye molecules is 5 nm. The refractive index of silver stearate is 1.515. The relative quantity calculation of the luminescent light passing from the molecules localized on the surfaces of silver stearate into the microcrystal of silver bromide was calculated by own software. The relative quantity of the luminescent light passing into silver halide via the lightguide mechanism is 0.0042.

However, the quantity of dye molecules placed on the particle of silver stearate is 30 to 50 times more than the quantity of dye molecules placed on the microcrystal of silver bromide. Consequently, 0.0042 is to be multiplied by 40. In this case, the contribution of dye molecules localized on the particle of silver stearate via the lightguide mechanism relative to the contribution of the dye molecules placed on the microcrystal of silver bromide is 0.17.

The investigations of silver stearate with adsorbed dye Rhodamine 6G by dielectric spectroscopy and differential scanning calorimetry showed a significant influence of dye adsorption on the properties of silver stearate (Castro et al. 2017a; 2017b; Smirnov et al. 2017). For example, the adsorption of Rhodamine 6G leads to an extreme increase of permittivity. This is probably due to the emergence of supplementary dipole–dipole interactions at the adsorption of silver stearate by Rhodamine 6G. The significant increase of permittivity enhances spectral sensitization via the lightguide mechanism.

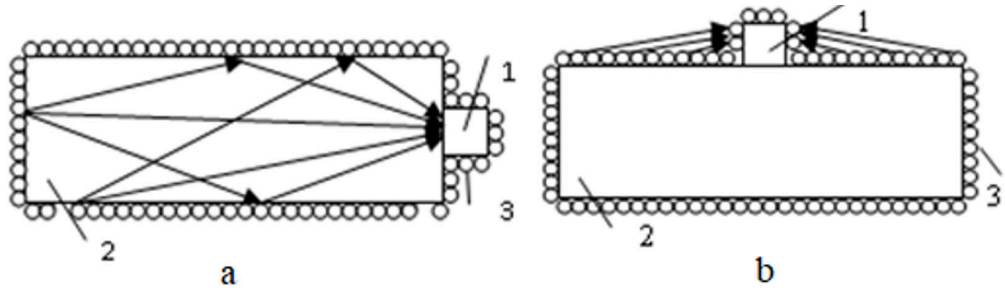

Fig. 1. The visual illustration of spectral sensitization by dyes adsorbed on the surface of silver stearate:
a—the lightguide mechanism, b—the direct hit of the luminescent light.
1 — silver halide, 2 — silver stearate, 3 — molecules of sensitizing dye

However, the lightguide mechanism does not make allowance for the potential influence of dye molecules localized on the surface of silver stearate particle containing the microcrystal of silver halide on spectral sensitization (Fig. 1*b*). The luminescent light emitted by these dye molecules may potentially hit into the lateral surfaces of the silver bromide microcrystal. The input data (the particle sizes etc.) for the calculation of this model are similar to the data used to calculate the lightguide mechanism model. In this case, the relative quantity of the luminescent light passing into the microcrystal of silver halide is 0.052. Then, we calculated the ratio of the quantity of dye molecules localized on the microcrystal of silver halide lateral face and the quantity of dye molecules localized on the surface of the silver stearate particle. Optimally, this relation is calculated as the ratio of surfaces area of the silver halide and silver stearate particles, i.e. $\frac{S''}{S^*} = \frac{S' - S}{5 \cdot S}$, where S′—the area of silver stearate surface where the microcrystal of silver bromide is placed, S—the area of silver bromide microcrystal surface, S″—the area of silver stearate surface without the area of silver halide microcrystal surface where the microcrystal of silver bromide is placed (the microcrystal of silver halide localizes on this face of the silver stearate particle). $S^* = 5 \cdot S$ (dye molecules localize on five surfaces of the silver halide particle). After the substitution it turned out that the quantity of dye molecules placed on silver stearate plane is 10 times more than the quantity of dye molecules placed on the microcrystal of silver halide. Therefore, the contribution of dye molecules localized on the silver stearate plane relative to dye molecules localized on the silver halide microcrystal is 0.52.

The total contribution estimation of dye molecules placed on the particle of silver stearate in relation to the contribution of dye molecules placed on the microcrystal of silver halide has to take into account relative contributions of the two described mechanisms and the multiplication of the given result by luminescence quantum yield of dye adsorbed on silver stearate. The luminescence quantum yield of Rhodamine 6G adsorbed on silver stearate is 0.55. In this case, the value of the contribution of dye molecules localized on silver stearate is 0.38, i.e., approximately 40 percent in relation to the contribution of dye molecules placed on the microcrystal of silver halide.

It is worth noting that the contribution value of dye molecules placed on the surface of silver stearate depends on the dye type because luminescence quantum yield is conditioned by the sort of dye adsorbed on the particle of silver stearate. If luminescence quantum yield of a dye is about 1.0 then the considered contribution is more than 60% in relation to the contribution of this dye adsorbed on the microcrystal of silver bromide.

Conclusion

The calculations show that the contribution of dye molecules localized on the particle of silver stearate to spectral sensitization of silver stearatesilver bromide structure is comparable to the contribution of dye molecules placed on the microcrystal of silver bromide. The effectiveness of spectral sensitization of photothermographic materials can be increased by 40 to 60 percent by the dye molecules adsorbed on the silver stearate particles. This is conditioned by both the lightguide mechanism and the direct hit of the luminescent light from dye molecules localized near the microcrystal of silver bromide. These calculations have confirmed the results of the investigations of photothermographic materials spectral sensitivity and absorption spectra of adsorbed dyes which showed comparable contributions

 https://www.doi.org/10.33910/2687-153X-2021-2-3-110-114

of dye molecules placed on the particles of silver stearate and dye molecules localized on the microcrystal of silver bromide (Goryaev 1998).

Conflict of interest

Authors declare that they have no conflict of interest.

Author contributions

A. A. Luzkov: The development of the calculation software for the estimation of the contribution of dye molecules localized on the surface of silver stearate to spectral sensitization in photothermographic materials. M. A. Goryaev and A. P. Smirnov: The formulation of the problem and analysis of the calculated results.

References

Akimov, I. A., Cherkasov, Yu. A., Cherkashin, M. I. (1980) *Sensibilizirovannyj fotoeffekt [Sensitized photoeffect]*. Moscow: Nauka Publ., 384 p. (In Russian)

Castro, R. A., Goryaev, M. A., Smirnov, A. P. (2017a) Dielectric properties and structural features of "silver stearate — adsorbed dye rhodamine 6G'" system. *Smart Nanocomposites*, 8 (2), 315–317. (In English)

Castro, R. A., Goryaev, M. A., Smirnov, A. P. (2017b) Non-Debye dielectric response in monolithic layers of silver stearate. *Physics of the Solid State*, 59 (2), 262–267. https://doi.org/10.1134/S106378341702010X (In English)

Ermolaev, V. L., Sveshnikova, E. B., Bodunov, E. N. (1996) Inductive-resonant mechanism of nonradiative transitions in ions and molecules in condensed phase. *Physics-Uspehi*, 39 (3), 261–282. https://doi.org/10.1070/PU1996v039n03ABEH000137 (In English)

Goryaev, M. A. (1991) Termoproyavlyaemye fotomaterialy na osnove neorganicheskikh sistem [Thermally developped photographic materials based on non-organic systems]. *Zhurnal nauchnoj i prikladnoj fotografii*, 36 (5), 421–430. (In Russian)

Goryaev, M. A., Kolesova, T. B., Timokhina, M. N., Gulkova, I. M. (1992) Formirovanie fotograficheskikh svojstv termoproyavlyaemykh fotomaterialov na osnove solej serebra [Formation of the photographic properties of the photothermographic materials based on silver salt]. In: Yu. A. Vasilevskij et al. (eds.). *Tekhnologiya i svojstva materialov dlya zapisi informatsii [Technology and materials properties for data recording]*. Moscow: NII Khimfotoproekt Publ., pp. 67–77. (In Russian)

Goryaev, M. A. (1994a) Control of photochemical sensitivity of thermally developable silver materials. *Russian Journal of Applied Chemistry*, 67 (6), 858–860. (In English)

Goryaev, M. A. (1994b) Lightguide mechanism of spectral sensitization of photoprocesses with dyes in an insolator-semiconductor system. *Soviet Technical Physics Letters*, 20 (11), 871–872. (In English)

Goryaev, M. A., Shapiro, B. I. (1997) Sensibilizatsiya serebryanykh termoproyavlyaemykh fotomaterialov v blizhnej infrakrasnoj oblasti [Sensitization of silver heat-developable materials to the near-IR range]. *Zhurnal nauchnoj i prikladnoj fotografii*, 42 (2), 65–67. (In Russian)

Goryaev, M. A. (1998) Dopolnitel'nye puti povysheniya effektivnosti spektral'noj sensibilizatsii fototermograficheskikh sistem [Additional ways for enhancing spectral sensitization of photothermographic materials]. *Zhurnal nauchnoj i prikladnoj fotografii*, 43 (3), 1–8. (In Russian)

Goryaev, M. A., Smirnov, A. P. (2012) Spektral'naya sensibilizatsiya fototermograficheskikh materialov i opticheskie svojstva stearata serebra [The spectral sensitization of photothermographic materials and the optical properties of silver stearate]. *Izvestia Rossijskogo gosudarstvennogo pedagogicheskogo universiteta im. A. I. Gertsena — Izvestia: Herzen University Journal of Humanities & Sciences*, 144, 29–36. (In Russian).

Goryaev, M. A. (2015) Dye sensitization of photoconductivity of polycrystalline silicon. *Russian Journal Physical Chemistry A*, 89 (12), 2320–2321. https://doi.org/10.1134/S0036024415120146 (In English)

Goryaev, M. A. (2016) Sensitized photoconductivity in silicon. In: *13th International scientific-technical conference on actual problems of electronic instrument engineering (APEIE)*. Novosibirsk: IEEE Publ., pp. 24–26. https://doi.org/10.1109/APEIE.2016.7802242 (In English)

Goryaev, M. A. (2018) Sensitized photovoltaic effect in silicon. In: *14th International scientific-technical conference on actual problems of electronic instrument engineering (APEIE)*. Novosibirsk: IEEE Publ., pp. 13–15. https://doi.org/10.1109/APEIE.2018.8545466 (In English)

Goryaev, M. A. (2019) Spectral sensitization of photo-EMF in monocrystalline silicon. *Optics and Spectroscopy*, 127 (1), 167–169. https://doi.org/10.1134/S0030400X19070087 (In English)

Goryaev, M. A., Smirnov, A. P. (2020a) Dye sensitizated photoprocesses in "silver stearate — silver bromide" system. *Physics of Complex Systems*, 1 (1), 10–14. https://doi.org/10.33910/2687-153X-2020-1-1-10-14 (In English)

Goryaev, M. A., Smirnov, A. P. (2020b) Luminescence of organic sensitizing dyes adsorbed on silver stearate. *AIP Conference Proceedings*, 2308 (1), article 030007. https://doi.org/10.1063/5.0035225 (In English)

Gratzel, M. (2003) Dye-sensitized solar cells. *Journal of Photochemistry and Photobiology C: Photochemistry Reviews*, 4 (2), 145–153. https://doi.org/10.1016/S1389-5567(03)00026-1 (In English)

James, T. H. (1977) *The theory of the photographic process*. New York: Macmillan Publ., 562 p. (In English)

Kabanov, V. A. (ed.). (1974) *Entsiklopediya polimerov. T. 2: L — Polinoznye volokna [Polymer encyclopedia. Vol. 2: L — Polynosic viscose rayon fiber]*. Leningrad: Sovetskaya entsiklopediya Publ., 1032 columns. (In Russian)

Morgan, D. A. (1993) 3M's dry silver technology — an ideal medium for electronic imaging. *The Journal of Photographic Science*, 41 (3), 108–109. https://doi.org/10.1080/00223638.1993.11738502 (In English)

Sahyun, M. R. V. (1998) Thermally developable photographic materials (TDPM): A review of the state-of-the-art in mechanistic understanding. *Journal of Imaging Science and Technology*, 42 (1), 23–30. (In English)

Smirnov, A. P., Castro, R. A., Goryaev, M. A., Fomicheva, E. E. (2017) Dielectric relaxation and charge transfer in silver stearate with adsorbed dye Rhodamine 6G layers. *Universitetskij nauchnyj zhurnal — Humanities and Science University Journal*, 27, 69–77. (In English)

Condensed Matter Physics.
Semiconductor Physics

UDC 538.9+535.3 https://www.doi.org/10.33910/2687-153X-2021-2-3-115-121

Effect of doping of molybdenum on the optical properties of glasses of the As—S system

P. S. Provotorov✉[1], V. T. Avanesyan[1], M. Krbal[2], A. V. Kolobov[1]

[1] Herzen State Pedagogical University of Russia, 48 Moika Emb., Saint Petersburg 191186, Russia
[2] Center of Materials and Nanotechnologies, University of Pardubice,
95 Studentská, 532 10 Pardubice 2, Czech Republic

Authors

Pavel S. Provotorov, ORCID: 0000-0003-1117-5431, e-mail: p.provotorov95@yandex.ru

Vachagan T. Avanesyan, ORCID: 0000-0001-5772-8375, e-mail: avanesyan@mail.ru

Milos Krbal, ORCID: 0000-0002-8317-924X

Alexander V. Kolobov, ORCID: 0000-0002-8125-1172

For citation: Provotorov, P. S., Avanesyan, V. T., Krbal, M., Kolobov, A. V. (2021) Effect of doping of molybdenum on the optical properties of glasses of the As-S system. *Physics of Complex Systems*, 2 (3), 115–121. https://www.doi.org/10.33910/2687-153X-2021-2-3-115-121

Received 31 May 2021; reviewed 28 June 2021; accepted 2 July 2021.

Funding: This work has been performed within a joint Russian-Czech project founded by Russian Foundation for Basic Research (grant 19-53-26017) and Czech Science Foundation (grant 20-23392J).

Abstract. This article discusses the spectral dependences of the absorption coefficient of thin arsenic sulphide films obtained by spin-coating, identified using a single-beam spectrophotometer in the wavelength range of 400–1000 nm. The effect of doping of molybdenum on the optical band gap is studied. While for a pure glass the band gap decreases with higher sulphur concentration, the opposite trend is observed in glass doped with molybdenum. Molybdenum doping also leads to an increase in Urbach energy. The obtained experimental curves are compared with theoretical ab-initio calculations.

Keywords: arsenic sulfide, molybdenum, spin-coating, optical band gap, Urbach energy.

Introduction

Glasses containing sulphur (S), selenium (Se) or tellurium (Te) are known as chalcogenide glassy semiconductors (ChGS). One of the features of ChGS is their ability to change properties under the influence of external factors (Kolobov 2006). In particular, this is due to the fact that in ChGS, along with the valence electrons involved in the formation of the covalent bond, there are pairs of electrons—the so-called lone electron pairs (LP-electrons)—the electronic states of which are located at the top of the valence band. This determines their response to the electronic excitation of the system (Kastner et al. 1976). Currently, these glasses are widely used in devices of infrared and integral optics, optical imaging and optical data processing due to their unique properties. The creation of stable and durable glasses with certain optical and electrical properties is an important goal for the physics of condensed state. Structural modification by varying the composition of a material is one of the ways to achieve this.

In practice, either binary compounds (Ge—Te, Sb—Te) or multicomponent ChGS systems such as (As—Se—S, Ge—As—S) are used. One of the most studied is the compound of arsenic sulphide As—S. It can be assumed that modifying this composition by molybdenum makes it is possible to vary its

structural features. Since the atoms of transition metals have six-fold coordination, the bonds are formed with empty *d*-orbitals of the metal and LP-electrons of chalcogenides. These are the so-called donor-acceptor bonds. As a consequence, the concentration of inert LP electrons in such materials decreases (Kolobov et al. 2020).

In this paper, we studied the optical characteristics of thin film of $As_xS_{(100-x)}$ (x = 15–40) composition, as well as the impact of the transition metal molybdenum on the optical properties. The choice of molybdenum is due to the fact that molybdenum disulphide MoS_2 is one of the most studied materials at present, and it is of interest to study the effects of doping of molybdenum on a typical sulphur-based ChGS. The paper also compares experimental data and the results of ab-initio modelling.

Experimental methods

Thin films with and without a transition metal: $As_xS_{(100-x)}$ and $As_xS_{(100-x)}$: Mo (x = 15–40) as samples. The films were obtained by spin-coating on a glass substrate. The thickness of the films was ~300 nm. The advantages of this method are as follows: the possibility to obtain uniform films over large areas of a given thickness and composition close to stoichiometric, at a low cost of equipment (Krbal et al. 2007). The doping of arsenic sulphide with a transition metal was carried out by adding a $(NH_4)_2MoS_4$ dissolved in propylamine. This solution was mixed with As—S solutions. The study of the morphology and composition of the films under consideration was carried out using a scanning electron microscope (SEM).

Transmission and reflection spectra were measured using a single-beam spectrophotometer SF-2000 in the wavelength range λ = 400–1000 nm in 1 nm increments.

Ab-initio simulations were performed using the CASTEP software (Clark et al. 2005).

Results and discussion

Figures 1 and 2 show the spectrophotometry results of the thin films of arsenic sulphide $As_xS_{(100-x)}$ and those containing molybdenum Mo, respectively. Three notable regions can be identified in the transmission spectra: strong absorption in the region of short wavelengths, transparency in the long-wavelength region and—between them—the fundamental absorption edge. The obtained high transmittance region (~70–80%) spectra have an oscillatory character, due to the presence of light interference in the film-substrate system.

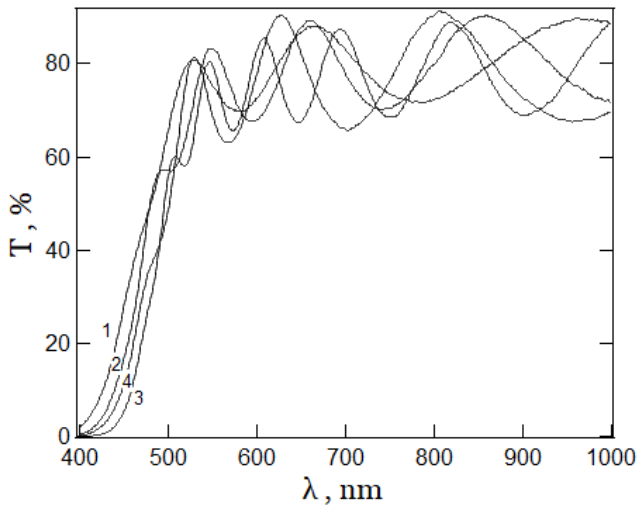

Fig. 1. Transmission spectra of As—S chalcogenide films with compositions:
$As_{15}S_{85}$ (1), $As_{20}S_{80}$(2) $As_{30}S_{70}$(3) $As_{33}S_{67}$(4)

 https://www.doi.org/10.33910/2687-153X-2021-2-3-115-121

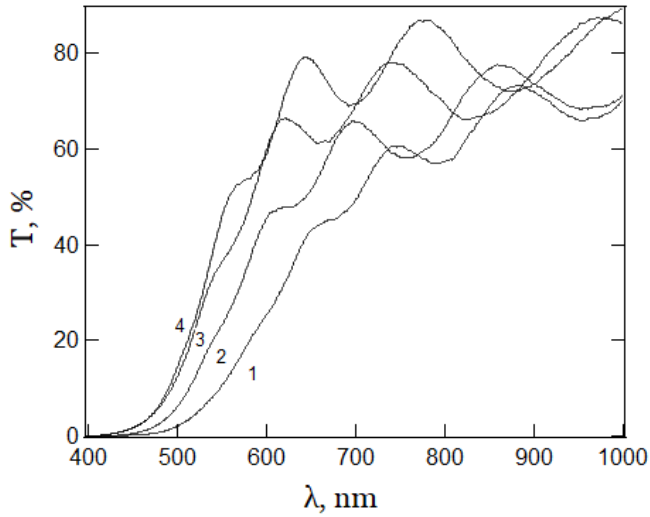

Fig. 2. Transmission spectra of As—S:Mo chalcogenide films with compositions: $As_{25}S_{75}$ (1), $As_{30}S_{70}$(2) $As_{33}S_{67}$(3) $As_{40}S_{60}$(4)

It is interesting to note that with an increase in sulphur concentration in the As—S system, the fundamental absorption edge shifts towards longer waves; however, in the presence of a transition metal in the film, the shift occurs towards shorter wavelengths.

In the region of strong absorption, for the dominant indirect allowed optical transitions characteristic of arsenic sulphide, the optical band gap E_{gopt} is related to the absorption coefficient α by Tauc extrapolation (Tauc et al. 1966):

$$\alpha h\nu = A\,(h\nu - E_g)^2, \tag{1}$$

where, A is a constant depending on the nature of optical transitions. Previously, this approach has been successfully used in particular in (Lazarenko et al. 2019) to study a compound of Ge—Sb—Te system.

The dependences of the expression $(\alpha h\nu)^{1/2}$ on the photon energy (Figures 3; 4) are characterized by linearity in the region of strong absorption ($\alpha \sim 10^4$ см$^{-1}$). Extrapolation of the tangent in this area to the intersection with the horizontal axis allowed us to determine the values of the optical band gap E_{gopt} (Table 1). The table demonstrates that, in an arsenic sulphide film without a transition metal, the band gap decreases with increasing sulphur content, while in the composition with molybdenum, the gap increases when the concentration of sulphur is increased. It is also seen that doping of a transition metal significantly reduces the band gap.

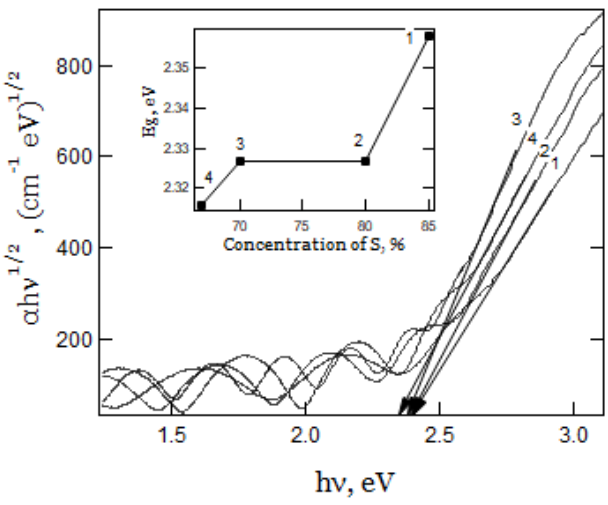

Fig. 3. Dependence of $(\alpha h\nu)^{1/2}$ on photon energy $h\nu$ in chalcogenide glasses As—S with composition: $As_{15}S_{85}$ (1), $As_{20}S_{80}$(2) $As_{30}S_{70}$(3) $As_{33}S_{67}$(4) from which the optical gap E_{gopt} is determined

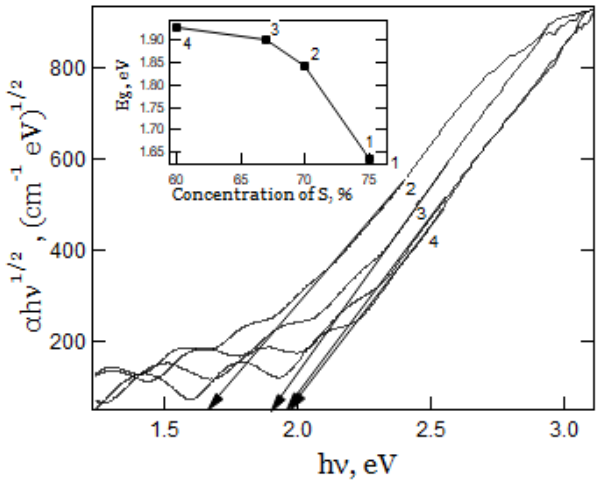

Fig. 4. Dependence of $(\alpha h\nu)^{1/2}$ on photon energy $h\nu$ in chalcogenide glasses As—S:Mo with composition: $As_{25}S_{75}$ (1), $As_{30}S_{70}$(2) $As_{33}S_{67}$(3) $As_{40}S_{60}$(4) from which the optical gap E_{gopt} is determined

Table 1. Optical parameters

Film composition	Optical band gap As—S, E_{gopt}, *eV*	Optical band gap As—S: Mo, E_{gopt}, *eV*	Urbach energy As—S, E_u, *eV*	Urbach energy As—S: Mo, E_u, *eV*
$As_{15}S_{85}$	2.3579	–	0.121	–
$As_{20}S_{80}$	2.3268	–	0.143	–
$As_{25}S_{75}$	–	1.6346	–	0.249
$As_{30}S_{70}$	2.3266	1.8422	0.122	0.143
$As_{33}S_{67}$	2.3158	1.9009	0.077	0.19
$As_{40}S_{60}$	–	1.9293	–	0.21

For glassy compounds, an exponential change in the absorption coefficient is often observed around the absorption edge. This dependence is often called an Urbach edge (Urbach 1953), and is described by the expression:

$$\alpha(h\nu) = \alpha_o \exp - [(E_{gopt} - h\nu) / E_U)], \quad (2)$$

where E_U is the characteristic Urbach energy corresponding to the depth of penetration of the "tail" of localized states into the forbidden band.

The values of Urbach energy calculated from the slope of the linear section of the dependence ln (α) on the photon energy (Fig. 5; 6) for the samples under consideration are presented in Table 1. The obtained values of Urbach energy are higher than typical (Mott, Davis 1979) by the order of ~0.05 eV. We believe that this may be due to the technology we used to obtain samples and the presence of uncontrolled residues of solvents.

 https://www.doi.org/10.33910/2687-153X-2021-2-3-115-121

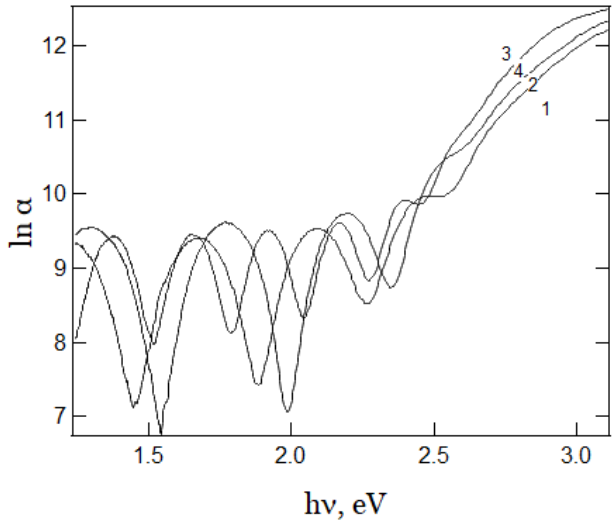

Fig. 5. The dependence of the absorption coefficient logarithm (ln α) on the photon energy *hν* in chalcogenide glasses As-S of composition: $As_{15}S_{85}$ (1), $As_{20}S_{80}$(2) $As_{30}S_{70}$(3) $As_{33}S_{67}$(4) from which the Urbach energy E_U is determined.

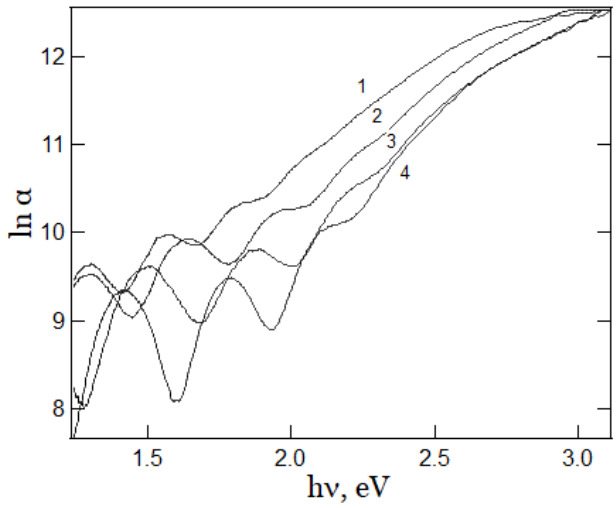

Fig. 6. Dependence of the logarithm of the absorption coefficient (ln α) on the photon energy *hν* in chalcogenide glasses As—S of composition: $As_{25}S_{75}$ (1), $As_{30}S_{70}$(2) $As_{33}S_{67}$(3) $As_{40}S_{60}$(4) from which the Urbach energy E_U is determined.

In parallel with the experimental study, the optical parameters of amorphous As_2S_3 (with and without molybdenum) were calculated in an ab-initio simulation based on the density functional theory. Figure 7 shows the calculated spectral dependences of the absorption coefficient. Note the absorption spectrum of As_2S_3 doped with molybdenum is shifted towards lower energies, which corresponds to a decrease in the band gap upon doping and is in agreement with experiment. The calculated value of the band gap is less than the corresponding experimental values, which is a well-known feature of such DFT calculations (Perdew 1985).

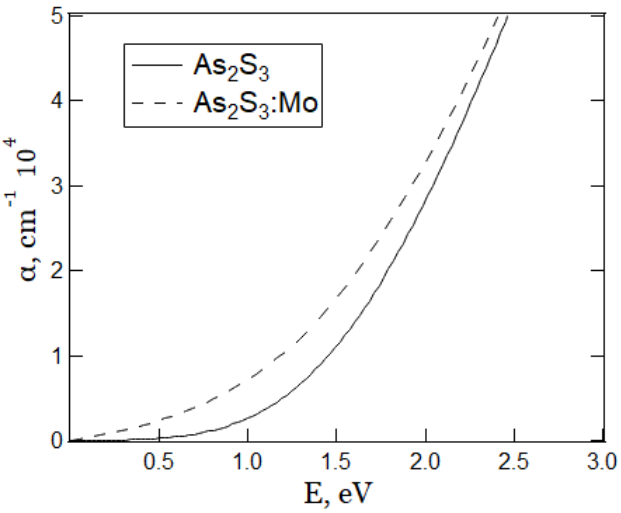

Fig. 7. Spectral dependence of the absorption coefficient obtained by DFT calculation

Conclusion

Thus, the study of the spectral dependences of the absorption coefficient of thin glassy films of the As—S system obtained by the spin-coating method made it possible to determine the values of the optical band gap, which correlate with the results of studies of films obtained by different methods (Němec et al. 2005; Yamaguchi 1985). It was shown that doping of the transition metal leads to a significant decrease in the band gap, as well as to the inversion of the compositional dependence of the band gap. Specifically, in a pure sample the optical gap increased with an increase in the ratio of sulphur in the composition, in samples containing molybdenum it decreased with an increase in sulphur. The experimentally observed decrease in the band gap with the introduction of molybdenum is confirmed by calculations from ab-initio.

Author contributions

Provotorov—conducting experiments, writing the article, Avanesyan—discussion of results, Krbal—making samples, Kolobov—performing DFT calculations, writing the article.

All authors discussed the final work.

References

Clark, S. J., Segall, M. D., Pickard, C. J. et al. (2005) First principles methods using CASTEP. Zeitschrift für Kristallographie. *Crystalline Materials*, 220 (5-6), 567–570. https://doi.org/10.1524/zkri.220.5.567.65075 (In English)

Kastner, M., Adler, D., Fritzsche, H. (1976) Valence-alternation model for localized gap states in lone-pair semiconductors. *Physical Review Letters*, 37 (22), article 1504. https://doi.org/10.1103/PhysRevLett.37.1504 (In English)

Kolobov, A. V. (ed.). (2006) *Photo-induced metastability in amorphous semiconductors.* Berlin: John Wiley & Sons Publ., 412 p. https://www.doi.org/10.1002/9783527602544 (In English)

Kolobov, A. V., Saito, Y., Fons, P., Krbal, M. (2020) Structural metastability in chalcogenide semiconductors: The role of chemical bonding. *Physica Status Solidi (B),* 257 (11), article 2000138. https://doi.org/10.1002/pssb.202000138 (In English)

Krbal, M., Wagner, T., Kohoutek, T. et al. (2007) The comparison of Ag–As33S67 films prepared by thermal evaporation (TE), spin-coating (SC) and a pulsed laser deposition (PLD). *Journal of Physics and Chemistry of Solids*, 68 (5-6), 953–957. https://doi.org/10.1016/j.jpcs.2007.03.036 (In English)

Lazarenko, P. I., Vorob'yev, Yu. V., Fedyanina, M. Ye. et al. (2019) Osobennosti opredeleniya opticheskoj shiriny zapreshchennoj zony tonkikh plenok materialov fazovoj pamyati [Particularities of estimating the optical band gap of the phase change memory thin films]. *Perspektivnye materialy*, 10, 14–25. https://doi.org/10.30791/1028-978X-2019-10-14-25 (In Russian)

Mott, N. F., Davis, E. A. (1979) *Electronic processes in non-crystalline materials.* 2nd ed. Oxford: Clarendon Press; New York: Oxford University Press, 608 p. (In English)

Němec, P., Jedelský, J., Frumar, M. et al. (2005) Structure of pulsed-laser deposited arsenic-rich As–S amorphous thin films, and effect of light and temperature. *Journal of Non-Crystalline Solids*, 351 (43-45), 3497–3502. https://doi.org/10.1016/j.jnoncrysol.2005.08.036 (In English)

Perdew, J. P. (1985) Density functional theory and the band gap problem. *International Journal of Quantum Chemistry*, 28 (S19), 497–523. https://doi.org/10.1002/qua.560280846 (In English)

Tauc, J., Grigorovici, R., Vancu, A. (1966) Optical properties and electronic structure of amorphous germanium. *Physica Status Solidi (B),* 15 (2), 627–637. https://doi.org/10.1002/pssb.19660150224 (In English)

Urbach, F. (1953) The long-wavelength edge of photographic sensitivity and of the electronic absorption of solids. *Physical Review*, 92 (5), article 1324. https://doi.org/10.1103/PhysRev.92.1324 (In English)

Yamaguchi, M. (1985) The relationship between optical gap and chemical composition in chalcogenide glasses. *Philosophical Magazine* B, 51 (6), 651–663. https://doi.org/10.1080/13642818508243153 (In English)

Theoretical Physics. Quantum Field Theory

UDC 530.182 https://www.doi.org/10.33910/2687-153X-2021-2-3-122-131

Spontaneous symmetry breaking and superposition of states in systems with dynamic chaos

A. V. Liaptsev✉[1]

[1] Herzen State Pedagogical University of Russia, 48 Moika Emb., Saint Petersburg 191186, Russia

Author

Alexander V. Liaptsev, ORCID: 0000-0002-8702-9062, e-mail: upm_eno@mail.ru

For citation: Liaptsev, A. V. (2021) Spontaneous symmetry breaking and superposition of states in systems with dynamic chaos. *Physics of Complex Systems*, 2 (3), 122–131. https://www.doi.org/10.33910/2687-153X-2021-2-3-122-131

Received 2 May 2021; reviewed 26 May 2021; accepted 26 May 2021.

Funding: The study did not receive any external funding.

Abstract. The article discusses one of the typical problems described by the equations of nonlinear dynamics—forced oscillations in a system with *W*-potential. It focuses, in particular, on chaotic oscillations in the presence of dissipation. In this case the state of the system is described by a chaotic (strange) attractor and can be characterized by the probability density in the phase space. A partial differential equation for the probability density is presented. It is shown that when the parameters change in the system under consideration, symmetry breaking can occur. In this case the superposition principle for the probability density is valid. It is similar to the superposition principle for the quantum mechanical function in the problem of particle motion in the *W*-potential field.

Keywords: nonlinear dynamics, strange attractor, probability density, chaos, perturbation theory, superposition principle.

Introduction

The phenomenon of spontaneous symmetry breaking is widespread in various physical systems, from the simplest mechanical systems to objects studied by cosmology. The essence of the phenomenon is that, despite the invariance of the equations of motion describing the system with respect to some transformations of symmetry, the system turns out to be in a state that is not invariant with respect to these transformations. For example, in the theory of molecular spectra, the Hamiltonian of a molecule is invariant under the operations of permutation of identical nuclei and inversion. The corresponding transformations form a complete permutation-inversion group of the nuclei of the molecule (Bunker 1979). However, in real molecules, some of the corresponding movements (permutation of the nuclei, or the movement leading to the inversion of the nuclei) are unrealizable. As a result, the actual symmetry of the molecule is lower than that of the original Hamiltonian. The symmetry group corresponding to the realized motion is defined by the Banker as the molecular symmetry group, which is a subgroup of the symmetry group of the original Hamiltonian.

A typical example is the tetratomic molecules AB_3, whose equilibrium structure of the nuclei is a tetrahedron with the base of a regular triangle (Fig. 1).

The combination of operations of inversion of nuclei and permutation of two identical nuclei results in the new configuration of the molecule, equivalent to the movement of the nucleus *A* through the plane formed by the nuclei *B*. This movement is realized in the NH_3 molecule, but it is not realized in the NF_3 molecule. As a result, the molecular symmetry group of the NH_3 molecule is isomorphic to the point symmetry group $\mathbf{D_{3h}}$, and the molecular symmetry group of the NF_3 molecule is isomorphic to the point symmetry group $\mathbf{C_{3v}}$ (Bunker 1979). Thus, one can say that in the NF_3 molecule the symmetry is broken, unlike in the NH_3 molecule.

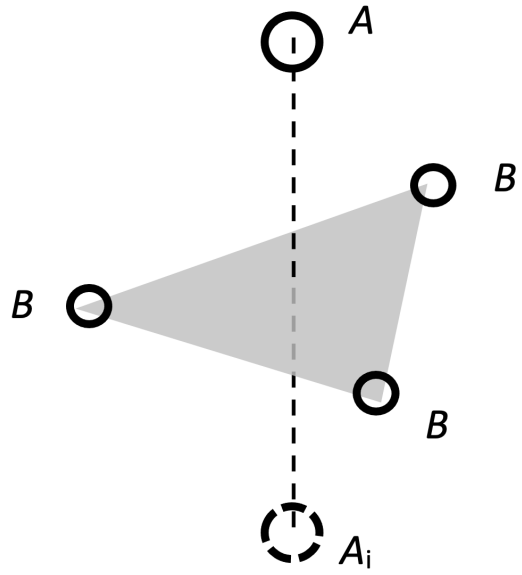

Fig. 1. Tunneling in a molecule AB_3

It should be noted, however, that if the NH_3 molecule is in the lowest vibrational states, then the motion considered above is low probable. In this case, we can talk about tunneling through the potential barrier when the nucleus *A* passes through the plane formed by the nuclei *B*. Taking into account the fact that the motion of the nuclei of a molecule can be considered in a quasi-classical approximation, the description of such tunneling is included in a number of textbooks as an educational task (Landau, Lifshitz 1977). The consequence of tunneling is the splitting of the energy level corresponding to the movement within a single minimum of energy (Fig. 2).

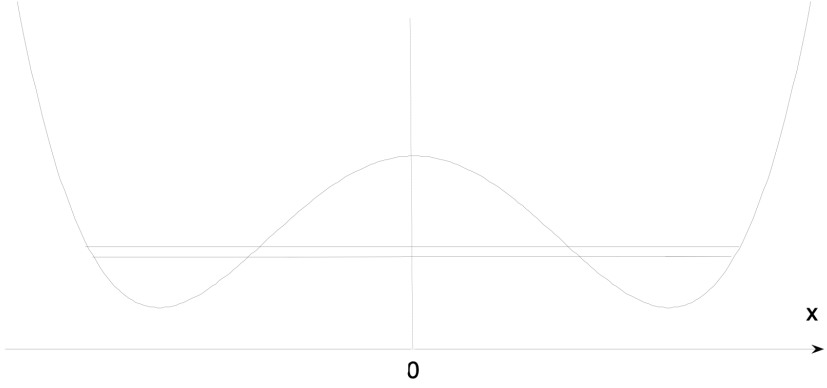

Fig. 2. Splitting in a system with *W*-potential due to tunneling

If we denote the wave function describing the motion in the region of one of the minima in disregard of tunneling through $\psi(x)$, then the wave functions corresponding to the split levels are superposition of the functions describing the motion in each of the corresponding pits:

$$\psi_{\pm}(x) = \frac{1}{\sqrt{2}}\left(\psi(x) \pm \psi(-x)\right).$$

The splitting of the energy levels ΔE is proportional to the tunneling probability. With a low probability, and, accordingly, a small splitting, the probability of detecting a molecule in the region of one of the local minima oscillates according to the law:

$$w = (\sin \Delta E t / \hbar)^2.$$

Since the oscillation period gradually increases with a decrease in the probability of tunneling, it is strictly impossible to determine at what specific value of ΔE the symmetry breaking occurred. In accordance with the definition of Bunker (Bunker 1979), we can assume that the symmetry is broken if the molecule remains in one of the configurations near the local minimum during the observation period. That is, the symmetry is broken at $\Delta E \lesssim t_{obs}/\hbar$, where t_{obs} is the observation time.

Chaotic motion in classical systems with W-potential

The potential shown in Fig. 2, usually called *W*-potential, can be modeled, in particular, by the expression:

$$U(x) = \frac{\alpha x^2}{2} + \frac{\beta x^4}{4},$$

where the parameters $\alpha < 0$ and $\beta > 0$. In classical mechanics, the motion of a body of a unit mass in such a potential in the presence of a viscous friction force and an external periodic force is described by the Duffing equation:

$$\ddot{x} = -\alpha x - \beta x^3 - \gamma \dot{x} + f \sin \omega t. \quad (1)$$

In this equation, the parameter γ characterizes the dissipation, and the parameters f and ω the amplitude and frequency of the external force.

Depending on the parameters of the problem, forced oscillations can capture the regions of both minima, or occur near one of the minima. At a sufficiently large value of the driving force f and a small depth of the pit $\Delta U = \frac{\alpha^2}{4\beta}$, the oscillation captures the regions of both minima, and with a decrease in f and (or) an increase in ΔU, it shifts to the region of one of the pits, without crossing the potential barrier.

A characteristic feature of the solutions of the Duffing equation is the occurrence of chaotic oscillations for certain sets of equation parameters. In the case of chaotic oscillations, the motion extends to both minima. In this case, the chaotic attractor has a certain symmetry, which is well shown in the fractal picture of the Poincare section (Liaptsev 2013). At the same time, with other sets of parameters, the movement can have a regular character, that is, be periodic. The system described by the Duffing equation with the parameter $\gamma > 0$ is a typical example of a dissipative system in which chaotic motion has certain features. Equation (1) can be written as an autonomous system of three differential equations of the 1st order:

$$\begin{aligned} \dot{x} &= v \\ \dot{v} &= -\alpha x - \beta x^2 - \gamma v + f \sin\varphi \\ \dot{\varphi} &= \omega \end{aligned} \quad (2)$$

The trajectory of the system in chaotic motion tends to the chaotic attractor (strange attractor). Since the dependence of the right side of equations (2) on the variable φ is determined by the periodic function, we can assume that $\varphi \in [0, 2\pi]$. The trajectory of motion in the phase space can be represented as a line "wound" on the torus (Fig. 3), and the Poincare section is a fractal (see, for example, (Schuster 1984)).

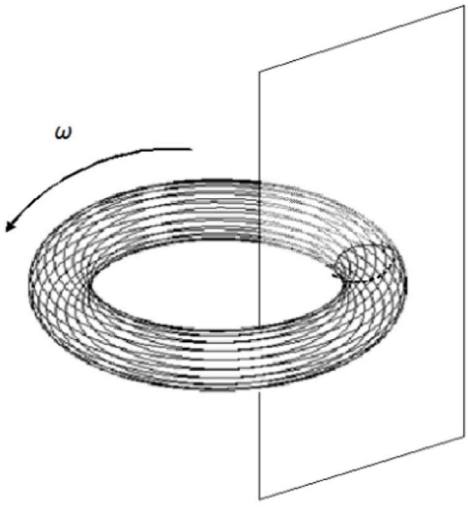

Fig. 3. Poincare cross section for the system (2)

 https://www.doi.org/10.33910/2687-153X-2021-2-3-122-131

The regularity of chaotic motion, which is clearly shown in the characteristic picture of the Poincare section allows us to introduce the probability density $\rho(\varphi,x,v)$, which determines the probability that the system is in the region of the phase space $d\varphi dxdv$ (Liapzev 2019; 2020):

$$dw = \rho\left(\varphi, x, v\right) d\varphi dxdv\,.$$

The probability density determined this way is normalized by one and satisfies the equation:

$$L\rho\left(\varphi, x, v\right) = 0\,, \tag{3}$$

where the differential operator L is defined by the expression:

$$L = \omega\frac{\partial}{\partial\varphi} + \frac{\partial}{\partial x} + \left(f\sin\varphi - \alpha x - \beta x^3 - \gamma\varphi\right)\frac{\partial}{\partial v}\,. \tag{4}$$

Equation (3), unlike the original Duffing equation (1), is a linear equation, so the probability density has properties characteristic of solutions of linear equations. In particular, for a small change in the operator L, the change in the probability density is also small. This allows us to use one or another version of the perturbation theory to calculate the average value of a certain physical quantity. That leads to the fact that if a change in the operator ΔL can be represented as a sum:

$$\Delta L = \sum\lambda_n \Delta L_n\,,$$

where λ_n are small parameters, then the average value of any physical quantity that depends on the variables φ, x, v, is also a linear function of these parameters. A numerical experiment for the case of specific perturbation operators confirms the validity of the above statement (Liapzev 2020).

It should be noted that such linear properties occur only for chaotic motion, when the attractor is a chaotic attractor, and changes in the parameters keep the motion chaotic. The probability density in this case can be modeled as some smooth function of the variables φ, x, v. In case of regular motion, the variables φ, x, v are periodic functions of time, and the attractor is a limit cycle with a period $2\pi n/\omega$, where n is a natural number. Within a single period, the variables x and v can be expressed as single-valued functions of the variable φ :

$$x = g\left(\varphi\right), \qquad v = h\left(\varphi\right)\,.$$

In accordance with equations (2), the functions $g(\varphi)$ and $h(\varphi)$ satisfy the equations:

$$\frac{dx}{d\varphi} = v\,,$$

$$\frac{dv}{d\varphi} = -\alpha x - \beta x^2 - \gamma v + f\sin\varphi\,.$$

The probability density in this case is no longer a smooth function, but can be expressed as the δ-functions:

$$\rho\left(\varphi, x, v\right) = C\delta(x - g(\varphi))\,\delta(v - h(\varphi))\,,$$

where C is the normalization coefficient. It is easy to show that the probability density determined in this way satisfies equation (3). However, small changes in the parameters of the equation in this case can lead to an abrupt change in the nature of the movement. As a result, with a small change in the parameters, the system may transfer to a new attractor in the form of a limit cycle or to a chaotic attractor.

Symmetry breaking for solutions of the Duffing equation

The potential corresponding to the conservative force in the Duffing equation is symmetric with respect to the coordinate inversion transformation. However, the equation of motion (1) itself does not have such a symmetry. Nevertheless, the symmetry is preserved if we use a set of transformations that leave equation (1) invariant:

$$x \to -x, \quad t \to t + 2\pi/\omega\,.$$

When moving from equation (1) to a system of autonomous equations (2), the set of transformations that leave this system invariant can be written as:

$$x \to -x, \quad v \to -v, \quad \varphi \to \varphi + \pi. \tag{5}$$

It is easy to see that the set of transformations (5) leaves the operator L, defined by equality (4), invariant. It follows from equation (3) that its solutions must be either even or odd functions with respect to the set of transformations (5). Since the probability density is by definition a positive value, we get the equation:

$$\rho(\varphi + \pi, -x, -v) = \rho(\varphi, x, v). \tag{6}$$

In the case of the W-potential, the probability density satisfies the relation (6) if the oscillations capture the regions of both minima. However, when the amplitude of the external field decreases, the oscillations are limited to either the region $x < 0$ or the region $x > 0$. This means that, depending on the initial conditions, one of the solutions exists: $\rho_<(\varphi, x, v)$, which turns to zero at $x > 0$, or $\rho_>(\varphi, x, v)$, which turns to zero at $x < 0$. The initial symmetry in this case manifests itself in the relations:

$$\rho_>(\varphi, x, v) = \rho_<(\varphi + \pi, -x, -v). \tag{7}$$

Let us now assume that for a certain set of parameters, the symmetry is broken, so that, depending on the initial conditions, the solutions $\rho_<(\varphi, x, v)$, or $\rho_>(\varphi, x, v)$, are realized, but the movements in both cases remain chaotic. Let us also assume that with some small change in the parameters, the symmetry is restored, and the character of the motion remains chaotic. This means that the symmetry breaking occurs when the operator L changes slightly. This, in turn, means that perturbation theory can be applied to find solutions. The case in question is similar to the quantum mechanical problem with W-potential. The solution for the probability density for chaotic oscillations involving both pits can be obtained from perturbation theory and in the zero order has the form:

$$\rho(\varphi, x, v) = \frac{1}{2}\left(\rho_<(\varphi, x, v) + \rho_<(\varphi + \pi, -x, -v)\right). \tag{8}$$

Thus, we can say that the principle of superposition of solutions is fulfilled, but, unlike the quantum mechanical problem, not for wave functions but for probability densities.

Numerical results

The validity of the above assumption can be verified by a numerical experiment. However, the attempt to use the solutions of the Duffing equations is unsuccessful. If, for some parameters, the oscillations are chaotic and capture the regions of both pits, that is, the transitions over the barrier realize, then when the symmetry is broken, the oscillation in the region of one of the pits turns out to be periodic, that is, instead of a chaotic attractor, the solution tends to the attractor in the form of a limit cycle. In this case, it is impossible to check the relation (8). The reason for the transition to the limit cycle is, apparently, that chaotic oscillations in the system described by the Duffing equation are realized either at large values of the amplitude of the driving force, or when there is a local maximum potential in the oscillation region. It is easy to show that for a quadratic potential, small oscillations, driving with harmonic force, can occur both in the case when the potential has a minimum (near the minimum) and in the case when the potential has a maximum (near the maximum). However, oscillations near the minimum are stable, and unstable near the maximum. Namely this kind of instability can generate chaotic motion.

The above considerations suggest that making the oscillations in the region of one of the pits chaotic when the symmetry is broken, it is necessary to complicate the shape of the potential by adding maxima to each of the pits. At the same time, it is desirable that for large values of the coordinate, the potential, like the potential in the Duffing equation, increases proportionally to the fourth power of the coordinate. In this paper, we used for the calculation the potential:

$$U(x) = x^4/4 + \alpha_0 Lor(x/\beta_0) + \alpha_1 Lor((x - dx)/\beta_1) + \alpha_1 Lor((x + dx)/\beta_1), \tag{9}$$

where the potential maxima are provided by the Lorentz distribution function:

$$Lor(x) = \frac{1}{1 + x^2}.$$

 https://www.doi.org/10.33910/2687-153X-2021-2-3-122-131

The parameters α_0 and α_1 determine the heights of the central and side local maxima, the parameters β_0 and β_1 determine the widths of these maxima, and the parameter dx determines the shift of the side maxima relative to the central maximum. For further calculations, the following values were used: $\alpha_0 = 7.5$, $\alpha_1 = 2.3$, $\beta_0 = \beta_1 = 0.3$, $dx = 1$. The potential graph is shown in Figure 4.

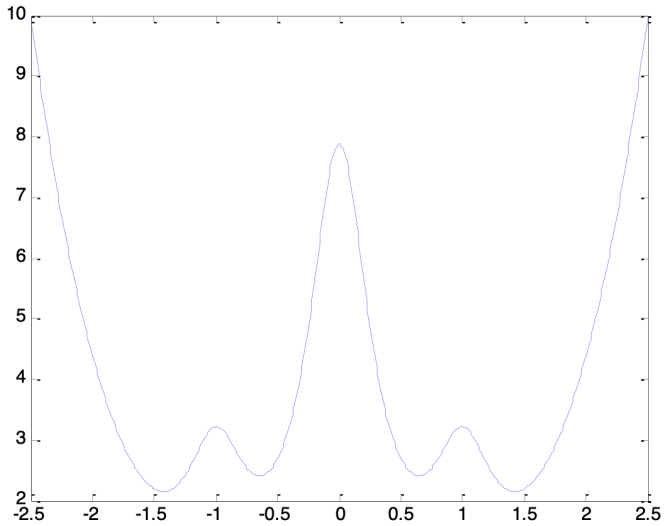

Fig. 4. Graph of the potential defined by the expression (9)

The numerical calculation was carried out for an equation similar to the Duffing equation, with a modified force:

$$\ddot{x} = F(x) - \gamma\dot{x} + f\sin\omega t\,,$$

where $F(x) = -\dfrac{\partial U}{\partial x}$ and $U(x)$ is defined by the expression (9). The parameters determining the dissipation and frequency of driving force were assumed to be equal, $\gamma = 0.2$, $\omega = 3.9$ respectively. The numerical calculation shows that at the value of the driving force amplitude $f = 1.85$, the oscillation at these parameter values is chaotic and captures the regions of both pits. Meanwhile, for quite long periods the oscillation occurs in one of the pits with rare jumps from one pit to another. For $f = 1.84$, a symmetry breaking occurs, so that the oscillation, which is also chaotic, is limited to the region of one of the pits, depending on the initial conditions.

The calculation of probability densities was carried out on a time interval equal to 10,000 periods of driving force. As a result of the calculation, a three-dimensional array $\rho(\varphi_i, x_j, v_k)$, was calculated. The array size is 120 × 101 × 101. The values of ϕ_i were distributed over the interval $[0,2\pi)$ in a regular way. The values of x_j and v_k were uniformly distributed over the intervals $[-x_{max}, x_{max}]$ and $[-v_{max}, v_{max}]$, respectively, where x_{max} and v_{max} are the maximum values of the coordinate and velocity modulus obtained as a result of calculations on this time interval.

Since the superposition principle is only statistically valid, an element-by-element comparison of the arrays included in equality (8) is meaningless. A visual comparison of the results can be illustrated by the graphs below.

The probability density averaged over the variable v

To graphically represent the probability density on a two-dimensional graph, we define the average density by the ratio:

$$\bar{\rho}(\varphi_i, x_j) = \frac{1}{N_v}\sum_{k=1}^{N_v}\rho(\varphi_i, x_j, v_k)\,,$$

where $N_v = 101$ is the dimension of the array along the v axis. Figure 5 shows graphs of the probability density $\bar{\rho}(\varphi_i, x_j)$ at $f = 1.84$, when the symmetry is broken, that is, oscillations occur in the region

of one of the pits depending on the initial conditions. On the horizontal axis, the x value is plotted, and on the vertical axis, the φ value is plotted. Darker areas correspond to a higher probability density.

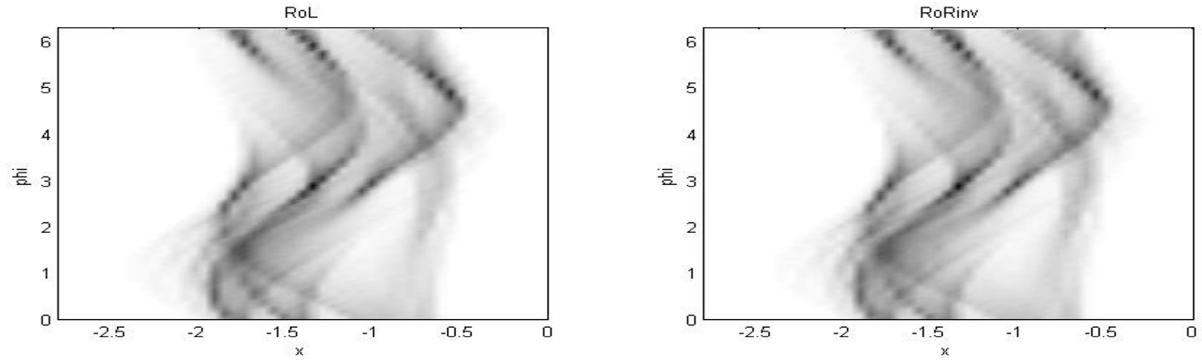

Fig. 5. Graphs of the average probability density (see the text)

The probability density distribution in the left graph corresponds to the oscillations in the left pit ($x < 0$). To clearly demonstrate the symmetry, the right graph shows the probability density of oscillations in the right pit ($x > 0$), transformed in accordance with the relations (5), that is, inverted with respect to x and shifted by π with respect to φ.

Figure 6 shows the probability density distribution graphs calculated at $f = 1.85$ (upper graph) and $f = 1.84$ (lower graph). To visually verify that the superposition principle is fulfilled, the probability density obtained for the left pit $\rho_{<}(\varphi, x, \upsilon)$, is shifted by π and inverted, after which the superposition (8) is calculated. Note that, due to the symmetry, an almost indistinguishable picture is obtained if instead of the relation (8) we use the relation:

$$\rho(\varphi, x,) = \frac{1}{2}\left(\rho_{<}(\varphi, x,) + \rho_{>}(\varphi, x,)\right).$$

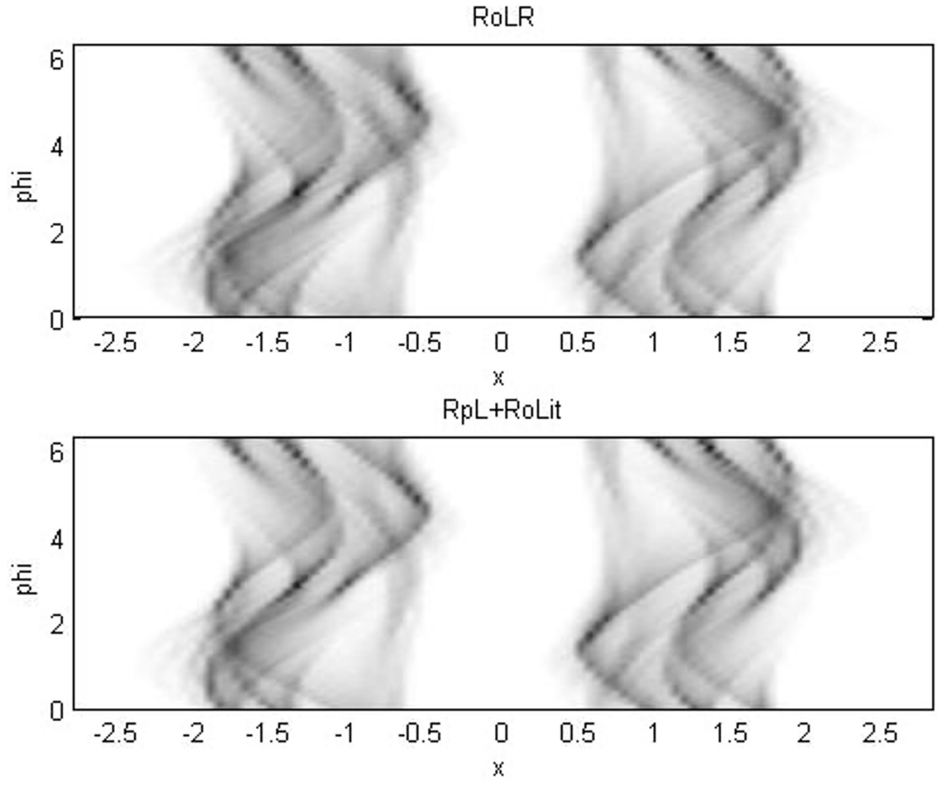

Fig. 6. Graphs of the average probability density (see the text)

 https://www.doi.org/10.33910/2687-153X-2021-2-3-122-131

Cross sections at ϕ = const

Other graphs that allow us to visually judge the fulfillment of relation (8) are the sections of the probability density graph at constant values of φ. Figure 7 shows the graphs at $\varphi = 0$ (left graphs) and $\varphi = \pi$ (right graphs).

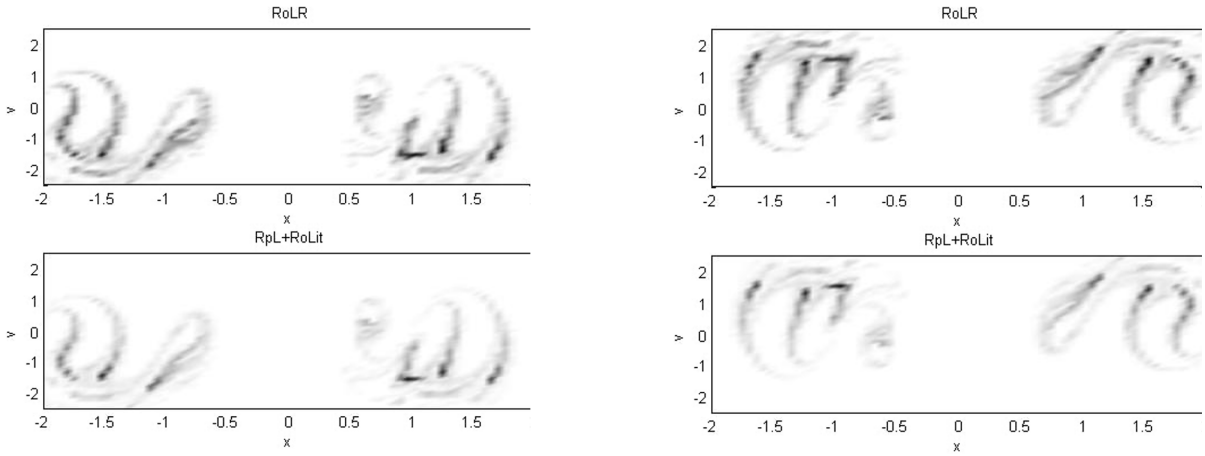

Fig. 7. Graphs of the probability density cross section (see the text)

As in the previous figures, the upper graphs correspond to the probability density calculated at $f = 1.85$, and the lower ones calculated at $f = 1.84$ for oscillations in the left pit and combined in accordance with the superposition principle (relation (8)). In addition to illustrating the superposition principle, the graphs also illustrate symmetry. Rotation of the right graphs by 180° around the axis perpendicular to the drawing plane (transformations $x \to -x$, $v \to -v$) gives an image that is almost indistinguishable from the left graphs.

Quantitative estimation of the results

To calculate a certain quantitative estimate of the fulfillment of the superposition principle, we turn to the equation for the probability density, which in the case of the potential chosen by us has the form:

$$\left(\omega\frac{\partial}{\partial\varphi}+\frac{\partial}{\partial x}+\left(f\sin\varphi-F\left(x\right)-\gamma v\right)\frac{\partial}{\partial v}\right)\rho\left(\varphi,x,v\right)=0\,, \tag{10}$$

where $F\left(x\right)=-\dfrac{\partial U}{\partial x}$, and $U(x)$ is defined by the expression (9). It is easy to show that if some positive function $\rho(\varphi, x, v)$, is found that satisfies equation (10), then for any real value p, the function $(\rho(\varphi, x, v))^p$, will also satisfy equation (10). Now, let us define the function:

$$\psi\left(\varphi,x,v\right)=\left(\rho\left(\varphi,x,v\right)\right)^{1/2}. \tag{11}$$

In the probabilistic sense, the function $\psi(\varphi, x, v)$ is analogous to the quantum mechanical wave function, its modulus square gives the probability density. However, first, the definition (11) does not allow us to uniquely define the function $\psi(\varphi, x, v)$, based on the function $\rho(\varphi, x, v)$. The function $\psi(\varphi, x, v)$ multiplied by an arbitrary phase factor depending on the variables φ, x, v, will also satisfy the relation $|\psi(\varphi, x, v)|^2 = \varrho(\varphi, x, v)$. Secondly, in this case, there are no properties similar to the properties of quantum mechanical wave function (quantization, interference, etc.). However, definition (11) can be used to quantify the proximity of two different solutions for the probability density. To do this, we can use the concept of a scalar product similar to the scalar product of quantum mechanical functions. For the two calculated probability densities $\rho_1(\varphi, x, v)$ and $\rho_2(\varphi, x, v)$, the scalar product of the corresponding functions $\psi_1(\varphi, x, v)$ and $\psi_2(\varphi, x, v)$ can be defined as follows:

$$\langle \psi_1 | \psi_2 \rangle = \frac{1}{N_\varphi N_x N_\upsilon} \sum_{i=1}^{N\varphi} \sum_{j=1}^{Nx} \sum_{k=1}^{N\upsilon} \psi_1 \left(\varphi_i, x_j, \upsilon_k \right) \psi_2 \left(\varphi_i, x_j, \upsilon_k \right), \quad (12)$$

where N_φ, N_x and N_υ determine the dimension of the array $\rho(\varphi_i, x_j, \upsilon_k)$. Obviously, the scalar product defined in this way can take a value from 0, when the probability densities are completely different, to 1, when the probability densities are completely the same. Thus, we can give the relations (7) and (8) some quantitative estimation. According to the relation (11), we define for the probability density $\rho_>(\varphi, x, \upsilon)$ the function $\psi_>(\varphi, x, \upsilon)$, and for the probability density $\rho_<(\varphi+\pi, -x, -\upsilon)$, the function $\psi_{<it}(\varphi, x, \upsilon)$. Calculated in accordance with the above definition, the scalar product gives the following value: $\langle \psi_> | \psi_{<it} \rangle \approx 0.98$. This quantitatively confirms the manifestation of the properties of symmetry presented in the above figures.

Similarly, to quantify the validity of the principle of superposition of solutions (8), we define for the probability density $\rho(\varphi, x, \upsilon)$ function $\psi(\varphi, x, \upsilon)$ according to the relation (11), and for the probability density $\frac{1}{2}\left(\rho_<(\varphi, x, \upsilon) + \rho_<(\varphi+\pi, -x, -\upsilon)\right)$ (the right part of equality (8)), the function $\psi_{superp}(\varphi, x, \upsilon)$. Then the numerical evaluation of the validity of the superposition principle can be determined by calculating the scalar product of the functions $\psi(\varphi, x, \upsilon)$ and $\psi_{superp}(\varphi, x, \upsilon)$ in accordance with the definition of the scalar product (12). The result of the calculations $\langle \psi | \psi_{superp} \rangle \approx 0.95$ corresponds to the similarity of the graphs shown in Figures 6 and 7.

The superposition principle in classical systems with dynamic chaos and in quantum mechanical systems

From the above, an analogy follows between the quantum mechanical problem, in which the symmetry breaking is considered, and the problem of classical dynamics, which admits a solution with dynamic chaos. Just as in a quantum mechanical problem, the use of the superposition principle (Feynman et al. 2006) can be justified by applying perturbation theory to the linear equation that determines the solution of the problem. Indeed, let equation (10), which can be written as:

$$L\rho(\varphi, x, \upsilon) = 0,$$

where

$$L = \omega \frac{\partial}{\partial \varphi} + \frac{\partial}{\partial x} + \left(f \sin\varphi - F(x) - \gamma \upsilon \right) \frac{\partial}{\partial \upsilon},$$

define the probability density of chaotic motion and have two solutions $\rho_<(\varphi, x, \upsilon)$ and $\rho_>(\varphi, x, \upsilon)$, which correspond to chaotic motion in the region of the left ($x < 0$) and right ($x > 0$) pits of a potential similar to W-potential (9). Due to the symmetry of the problem, the relation (7) holds. We will consider the operator L as an unperturbed operator. Let a small addition (perturbation):

$$V = \Delta f \sin\varphi \frac{\partial}{\partial \upsilon} \quad (13)$$

to the unperturbed operator lead to the fact that the solution of the equation

$$(L + V)\rho(\varphi, x, \upsilon) = 0$$

describes the chaotic movement that captures both pits. The solution $\rho(\varphi, x, \upsilon)$ in this case can be obtained by perturbation theory. In the zero approximation for $\rho(\varphi, x, \upsilon)$, we get the former equation. However, since the solution must now describe the motion in both pits, it is necessary to take a superposition of the solutions $\rho_<(\varphi, x, \upsilon)$ and $\rho_>(\varphi, x, \upsilon)$. The symmetry properties and positivity of the $\rho(\varphi, x, \upsilon)$ function allow us to obtain only the solution proportional to the sum of the solutions $\rho_<(\varphi, x, \upsilon)$ and $\rho_>(\varphi, x, \upsilon)$, and from the normalization condition it follows that the coefficient for the sum must be equal to 1/2.

The numerical experiment confirms the above relations. We have given just one concrete example. Calculations show that with an increase in the perturbation operator (13), that is, with an increase in the value of Δf, the corrections of the 1st order of the perturbation theory increase. This manifests itself in a decrease in the value of $\langle \psi_> | \psi_{<it} \rangle$.

The introduction of functions proportional to the root of the probability density is convenient for evaluating the accuracy of perturbation theory calculations. However, they cannot be given the same

 https://www.doi.org/10.33910/2687-153X-2021-2-3-122-131

meaning of wave functions as in a quantum mechanical problem. This statement can be illustrated by the following example. As mentioned above, in a quantum mechanical problem with *W*-potential, the probability of detecting a molecule in the region of one of the local minima oscillates according to the law expressed by:

$$w = (\sin \Delta Et / \hbar)^2 . \tag{14}$$

These oscillations are manifested in the spectra of the corresponding systems. In the classic problem under consideration, we also observe jumps from one pit to another with long intervals of chaotic motion in the region of each of the pits. However, the numerical experiment shows that there is no regular periodicity similar to the oscillations (14). This statement is confirmed by the fact that the calculated Fourier spectrum for such motions does not have any clearly expressed maximum, in addition to the maximum at the frequency of the driving force ω.

Conclusion

This paper investigated only one special case of chaotic motion in the problem of classical nonlinear dynamics, however, the obtained conclusions can be generalized to other systems where dynamic chaos manifests itself. These conclusions can be formulated as follows.

1) Chaotic motion in dissipative systems of classical dynamics can be characterized by the probability density of states in the phase space. The function corresponding to the probability density can be obtained by solving a partial differential equation.
2) For the solutions of this classic problem, the principle of superposition of solutions is valid, as is the case with the quantum mechanical problem.
3) The validity of the superposition principle can be most effectively shown in the problem that admits a symmetry breaking when changing some parameters. The validity is confirmed by the numerical experiment.

Conflict of interest

Author declares that there is no conflict of interest.

References

Bunker, P. R. (1979) *Molecular symmetry and spectroscopy*. New York: Academic Press, 440 p. (In English)

Feynman, R. P., Leighton, R. B., Sands, M. (2006) *The Feynman lectures on physics including Feynman's tips on physics: The definitive and extended edition. Vol. 2.* 2nd ed. Boston: Addison-Wesley Publ., 512 p. (In English)

Landau, L. D., Lifshitz, E. M. (1977) *Quantum mechanics: Non-relativistic theory. Vol. 3.* 3rd ed., rev. Oxford et al.: Pergamon Press, 688 p. (In English)

Liaptsev, A. V. (2013) Simmetriya regulyarnykh i khaoticheskikh dvizhenij v zadachakh nelinejnoj dinamiki. Uravnenie Duffinga [The symmetry of regular and chaotic motions in nonlinear dynamic problems. Duffing equation]. *Izvestia Rossijskogo gosudarstvennogo pedagogicheskogo universiteta im. A. I. Gertsena — Izvestia: Herzen University Journal of Humanities & Sciences*, 157, 24–34. (In Russian)

Liapzev, A. V. (2019) The calculation of the probability density in phase space of a chaotic system on the example of rotator in the harmonic field. *Computer Assisted Mathematics*, 1, 55–65. (In English)

Liapzev, A. V. (2020) Linear properties of chaotic states of systems described by equations of nonlinear dynamics. Analogy with quantum theory. *Physics of Complex Systems*, 1 (4), 150–157. https://doi.org/10.33910/2687-153X-2020-1-4-150-157 (In English)

Schuster, G. H. (1986) *Deterministic chaos. An introduction.* Weinheim: Physik-Verlag, 220 p. (In English)

Physics of the Atomic Nucleus and Elementary Particles. Elementary Particle Physics

UDC 539.1.07+539.1.05 https://www.doi.org/10.33910/2687-153X-2021-2-3-132-138

Comparison of some properties of charged pions in $p^{12}C$ and $n^{12}C$ collisions at 4.2 GeV/c

R. N. Bekmirzaev✉[1], X. Bekmirzaeva[1], Q. O. Khusniddin[2], M. Mustafaeva[1]

[1] Jizzax State Pedagogical Institute of Uzbekistan, 4 Sharof Rashidov Str., Jizzax 130100, Uzbekistan
[2] Physical-Technical Institute of the Academy of Sciences of the Republic of Uzbekistan, 2B Chingiz Aitmatov Str., Tashkent 100084, Uzbekistan

Authors

Rakhmatulla N. Bekmirzaev, ORCID: 0000-0003-4895-5765, e-mail: bekmirzaev@mail.ru

Xursanoy Bekmirzaeva, ORCID: 0000-0001-7740-8889, e-mail: bekmirzaeva@mail.ru

Khusniddin Q. Olimov, e-mail: olimov@uzsci.net

Marjona Mustafaeva, e-mail: marjona@mail.ru

For citation: Bekmirzaev, R. N., Bekmirzaeva, X., Khusniddin, Q. O., Mustafaeva, M. (2021) Comparison of some properties of charged pions in $p^{12}C$ and $n^{12}C$ collisions at 4.2 GeV/c. *Physics of Complex Systems*, 2 (3), 132–138. https://www.doi.org/10.33910/2687-153X-2021-2-3-132-138

Received 28 April 2021; reviewed 8 June 2021; accepted 8 June 2021.

Funding: The study did not receive any external funding.

Abstract. The new experimental data on various properties of the secondary charged pions produced in $n^{12}C$ collisions at 4.2 GeV/*c* are presented. A comparative analysis of the average multiplicities and various kinematic properties of the charged pions produced in $n^{12}C$ and $p^{12}C$ collisions at 4.2 GeV/*c*is is made. The experimental data are compared systematically with the predictions of the modified FRITIOF model. It is found that the modified FRITIOF model overestimates the average multiplicities of the charged pions in $n^{12}C$ ($p^{12}C$) collisions at 4.2 GeV/*c* compared to the experiment. It is shown that this is due to the fact that the model overestimates the contribution of the intranuclear cascade processes in production of pions in the target fragmentation region compared to the experiment. It is also found that the model underestimates the multiplicity of the charged pions in the projectile fragmentation region. It is shown that this is due to the fact that the model underestimates the contribution of Δ resonances decays to the generation of the fast charged pions in the analyzed collisions.

Keywords: neutron-carbon collisions, proton-carbon collisions, intermediate energies, pion production, average multiplicities, total and transverse momentum distributions, rapidity distributions, emission angle distributions.

Introduction

This paper builds upon a series of previous papers (Olimov et al. 2007a; 2007b) and is devoted to the comparative analysis of various properties of the charged pions produced in $p^{12}C$ and $n^{12}C$ collisions at 4.2 GeV/*c*. The experimental data are compared with the results of Monte Carlo calculations in the framework of the modified version of the FRITIOF model (Bekmirzaev et al. 1984; Galoyan et al. 2002).

The experiment was performed using a 2-meter propane (C_3H_8) bubble chamber at the Laboratory of High Energies of Joint Institute for Nuclear Research (JINR, Dubna, Russia). The bubble chamber was irradiated by the beams of protons, deuteron and helium-4 nuclei accelerated to the momentum of 4.2 GeV/*c* per nucleon at the Dubna Synchrophasotron. The experimental data consist of 6736 $p^{12}C$,

7071 d^{12}C, 11974 ^{4}He^{12}C, and 2798 n^{12}C inelastic collision events. n^{12}C collisions were selected from d^{12}C and ^{4}He^{12}C interactions according to the procedures described in detail in (Olimov et al. 2007b).

The procedures used to determine particle momenta with a track projection length in the working volume of the chamber $l < 4$ cm, as well as separation of protons and π^+ mesons in the momentum region p > 750 MeV/c are described in (Olimov et al. 2007a).

Experimental results and their discussion

Table 1 shows the experimental data on the average multiplicities of charged pions (the mean number of the charged pions per one inelastic collision event) produced in p^{12}C and n^{12}C collisions at 4.2 GeV/c.

From Table 1 one can see that the average multiplicity of negative (positive) pions coincides with the average multiplicity of positive (negative) pions in p^{12}C and n^{12}C collisions, respectively. This result is obvious from the isotopic invariance of the strong interactions under consideration. However, as seen from Table 1, the model overestimates the average multiplicities in comparison with the experimental data by approximately 10%, both for negative and positive pions.

Table 1. Average multiplicities of $\pi-$ and $\pi+$ mesons, as well as their absolute differences DR in the experiment and in the modified FRITIOF model in p^{12}C and n^{12}C collisions at 4.2 GeV/c

Quantity	Type of collision			
	p^{12}C		n^{12}C	
	Experiment	Model	Experiment	Model
$<n(\pi-)>$	0.36 ± 0.02	0.40 ± 0.01	0.64 ± 0.02	0.70 ± 0.01
$<n(\pi+)>$	0.63 ± 0.02	0.71 ± 0.01	0.37 ± 0.02	0.39 ± 0.01
ΔR	0.27 ± 0.03	0.31 ± 0.01	0.27 ± 0.03	0.31 ± 0.01

In order to determine the contribution of inelastic charge exchange reactions of the initial neutron (proton) to the formation of negative (positive) pions, let us consider the difference in the average multiplicities of the negative (positive) and positive (negative) pions in n^{12}C (p^{12}C) collisions (see the last line of Table 1). The numbers of protons and neutrons in the ^{12}C- nucleus are the same, so the contribution of inelastic charge exchange reactions of the target nucleons to the formation of both the negative and positive pions of the final state should be the same due to the isotopic invariance of the strong interactions. Then the value of DR can be used as an estimate of the contribution of inelastic charge exchange reactions of the initial neutron (proton) to the formation of the final state negative (positive) pions in n^{12}C (p^{12}C) collisions. One can see from the data in Table 1 that, both in the experiment and in the modified FRITIOF model (Azimov et al. 1976; Galoyan et al. 2002) these contributions are equal for both types of collisions, respectively. If we consider that in the experiment the value of the inelastic charge exchange coefficient of the nucleon in nucleon-nucleus collisions (i.e. the average multiplicity of the initial nucleon lost during the collision process) is equal to 0.36 ± 0.01 (Galoyan et al. 2002), then, as can be seen from Table 1, three-fourths (¾) of the inelastic charge exchange coefficient of the initial nucleon can be attributed to the formation of a single charged pion, and the remaining one-fourths (¼)of this coefficient can be attributed to charge exchange reactions with nucleons of the target of the $np \to pn$ or $pn \to np$ type. Hence, it can be concluded that more than 42% of the negative (positive) pions are produced due to inelastic charge exchange of the initial neutron (proton) in n^{12}C (p^{12}C) collisions at 4.2 GeV/c.

We have observed that our version of the modified FRITIOF model (Bekmirzaev et al. 1984; Botvina et al. 1993) overestimates the average multiplicities of the charged pions in the interactions considered. It is interesting to understand to what extent this discrepancy is reflected in the kinematic characteristics of the charged pions.

In Table 2, we present the experimental data on the mean values of the total, longitudinal and transverse momenta, emission angles, and the longitudinal rapidity in the laboratory frame, and the partial inelasticity coefficient for π^- and π^+ mesons produced in p^{12}C and n^{12}C collisions at 4.2 GeV/c in comparison with the results of model calculations.

It follows from Table 2 that the average values of the transverse momenta of the charged pions in the experiment coincide, within statistical errors, for p^{12}C and n^{12}C collisions. It can also be noted that the average values of the longitudinal momentum, as well as of the longitudinal rapidity for the negative (positive) pions are greater than those for positive (negative) pions in n^{12}C (p^{12}C) collisions, respectively. This difference can be explained, as noted above, if we take into account both the contributions of inelastic charge exchange reaction (conversion) of incident neutron (proton) into the proton (neutron) and the negative (positive) pions, and of the Δ^0 (Δ^+) resonance decays into the nucleon and pion. The average values of the longitudinal rapidity of the charged pions, calculated according to the modified FRITIOF model, coincide with the results of the experiment within statistical errors.

Table 2 also presents the experimental and theoretical values of the partial inelasticity coefficients for π^- and π^+ mesons produced in p^{12}C and n^{12}C collisions, respectively. It should be noted that since the value of the incident momentum and the mass of the projectile-nucleon in the experiment are comparable, we have calculated the partial inelasticity coefficients of the charged pions as the ratio of the total energy of the secondary charged pions in a given individual collision event to the kinetic energy of the projectile nucleon. Table 2 shows that the average values of the partial inelasticity coefficients for the charged pions coincide, within statistical errors, in the experiment and the model. This indicates that distribution of the primary (incident) energy among the produced pions, or the ratios of the main mechanisms for pion production, is indeed taken into account correctly in the model.

Table 2. Average values of the total, longitudinal and transverse momenta (in MeV/c), the emission angle (in degrees), the longitudinal rapidity and the partial inelasticity coefficient (K) for $\pi-$ and $\pi+$ mesons in p^{12}C and n^{12}C collisions at 4.2 GeV/c in the experiment and in the modified FRITIOF model

Quantity	Type of collision			
	p^{12}C		n^{12}C	
	Experiment	Model	Experiment	Model
$<P(\pi-)>$	501 ± 8	495 ± 3	575 ± 10	526 ± 2
$<P(\pi+)>$	571 ± 7	527 ± 2	511 ± 7	492 ± 3
$<Pl(\pi-)>$	395 ± 9	381 ± 3	464 ± 11	414 ± 3
$<Pl(\pi+)>$	454 ± 7	414 ± 2	386 ± 12	376 ± 3
$<Pt(\pi-)>$	243 ± 3	233 ± 1	245 ± 3	243 ± 1
$<Pt(\pi+)>$	263 ± 3	242 ± 1	262 ± 5	234 ± 1
$<Pt(\pi-)>$	48.0 ± 0.7	45.8 ± 0.2	43.6 ± 0.7	43.9 ± 0.2
$<Pt(\pi+)>$	46.2 ± 0.5	44.0 ± 0.2	47.7 ± 0.9	46.3 ± 0.2
$<Y(\pi-)>$	0.89 ± 0.02	0.92 ± 0.01	1.00 ± 0.02	0.97 ± 0.01
$<Y(\pi+)>$	0.95 ± 0.02	0.97 ± 0.01	0.88 ± 0.02	0.91 ± 0.01
$<K(\pi-)>$	0.06 ± 0.01	0.06 ± 0.001	0.12 ± 0.01	0.12 ± 0.01
$<K(\pi+)>$	0.11 ± 0.01	0.12 ± 0.01	0.06 ± 0.01	0.06 ± 0.01

It is important to understand which region of the momentum distributions is responsible for the discrepancy observed between the multiplicities of the charged pions in the experiment and the model. For this purpose, we consider, first of all, the total momentum distributions for the negative and positive pions in n^{12}C and p^{12}C collisions.

Figs. 1 and 2 show the total momentum distributions of π^- (a) and π^+ (b) mesons in n^{12}C (Fig. 1) and p^{12}C (Fig. 2) collisions at 4.2 GeV/*c*, normalized by the total number of inelastic events (N_{events}) and the width of the momentum interval (ΔP). The corresponding distributions calculated using the modified FRITIOF model are shown as histograms for comparison.

 https://www.doi.org/10.33910/2687-153X-2021-2-3-132-138

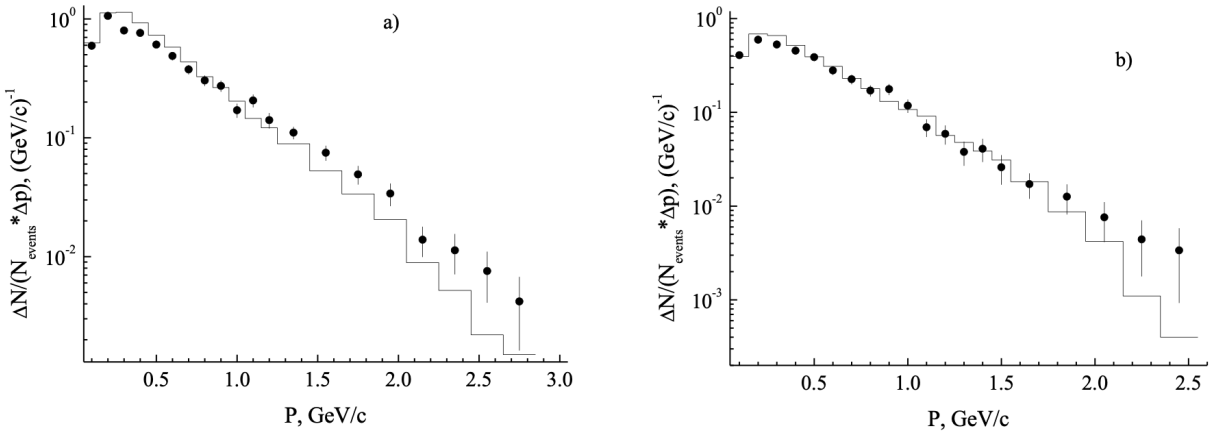

Fig. 1. The normalized total momentum distributions of the negative (a) and positive (b) pions in n^{12}C collisions at 4.2 GeV/c. Histograms–the calculations within the framework of the modified FRITIOF model (Bekmirzaev et al. 1984)

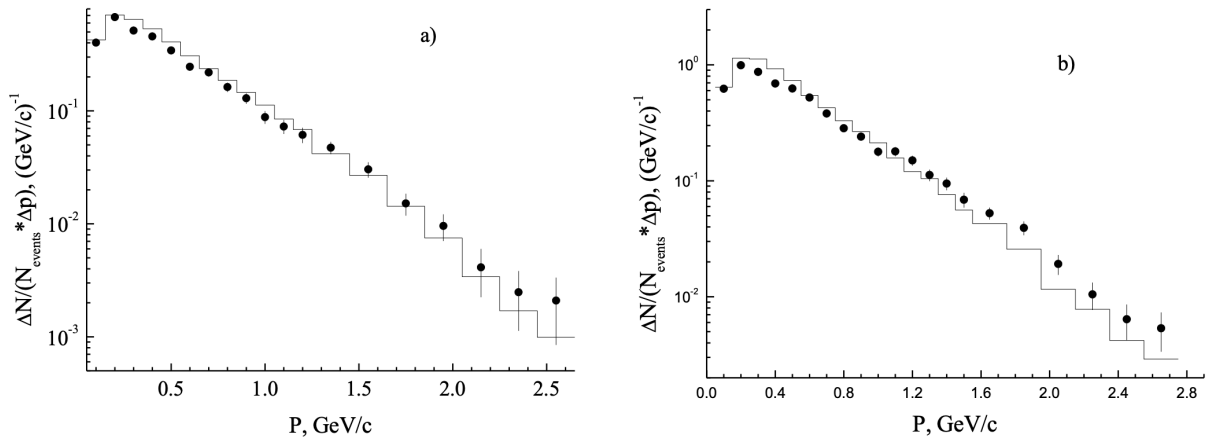

Fig. 2. The normalized total momentum distributions of the negative (a) and positive (b) pions in p^{12}C collisions. Histograms—the calculations within the framework of the modified FRITIOF model

We can see from Fig. 1 that the experimental momentum distribution of π^+ (b) mesons in n^{12}C collisions is a single-modal one, it demonstrates a smooth decrease with the pion momentum, and does not have any irregularities up to the largest values of the total momentum. Regarding the experimental spectrum of π^-(a) mesons in n^{12}C collisions, although in general it is similar to the spectrum of π^+ mesons, there is some deviation from the exponential dependence in the region of large momentum $p > 1$ GeV/c, where the spectrum decreases more slowly with the increase of the total momentum. This observed "shoulder" is probably related to the production of fast π^- mesons in n^{12}C collisions due to inelastic charge exchange reactions (conversions) of the incident neutron into the π^- meson and proton, and excitation of the incident neutron into intermediate Δ^0 resonance, which decays swiftly into the same channel: π^- meson and proton. It is important to note that, based on the kinematical considerations, the contribution of the leading delta resonance to the pion spectrum will be particularly noticeable in the region of the total momenta p^3 1 GeV/c.

The corresponding reverse pattern is observed for the momentum distributions of π^- (a) and π^+ (b) mesons in p^{12}C collisions in Fig. 2. Here, the irregularity in the momentum distribution of π^+ mesons can be caused both by the inelastic charge exchange reaction (conversion) of the incident proton into π^+ meson and neutron, and by the decay of the intermediate Δ^+ resonance formed due to excitation of the incident proton.

Figs. 1 and 2 also show that the calculated momentum spectra of the charged pions for both π^- (a) and π^+ (b) mesons are single-modal ones and there are no deviations from the general smooth behaviour of the spectra with the increase in momentum. The theoretical data exceed the experimental ones for both π^- (a) and π^+ (b) mesons for both types of collisions in the momentum range of $p \leq 1$ GeV/c. The model is apt to describe the shape of the experimental momentum distributions of the negative (positive) pions in n^{12}C (p^{12}C) collisions in the range $1 \leq p \leq 2$ GeV/c. Regarding the high momentum tail of the momentum distributions (p^3 1 GeV/c), the model systematically underestimates the negative (positive) pions in n^{12}C (p^{12}C) collisions when compared to the experimental data.

Hence, from comparison of the experimental data with model calculations we see that the modified FRITIOF model overestimates the average multiplicity of the charged pions in p^{12}C and n^{12}C collisions at 4.2 GeV/c by about 10%. It is important to mention that the model overestimates the number of pions in the target fragmentation region ($p \leq 1$ GeV/c) and underestimates their number (π^- mesons for n^{12}C collisions and π^+ mesons for p^{12}C collisions) in the projectile fragmentation region (p^3 1 GeV/c).

Thus, the 10% excess of the calculated values of the average multiplicity of the charged pions in the model in comparison with the experiment is due to the fact that the model overestimates the contribution of intranuclear cascade processes to the production of pions in the target fragmentation region. This ultimately leads to lower average values of the momentum of the charged pions in the modified FRITIOF model (Bekmirzaev et al. 1984) compared to the experiment. The average multiplicity of the protons with momenta $p > 140$ MeV/c (the lower detection threshold for the reliable registration of the protons in the experiment) in p^{12}C and n^{12}C collisions in the experiment and the model are as follows: $\langle n_p(n^{12}C)\rangle_{exp} = 1.65 \pm 0.02$, $\langle n_p(n^{12}C)\rangle_{mod} = 1.96 \pm 0.01$ and $\langle n_p(p^{12}C)\rangle_{exp} = 1.92 \pm 0.02$, $\langle n_p(p^{12}C)\rangle_{mod} = 2.32 \pm 0.01$. It can be seen that for both types of collisions the average multiplicity of protons is approximately 1.2 times greater in the model than in the experiment.

On the other hand, the fact that the model underestimates the number of pions in the region of projectile fragmentation, as well as the absence of a "shoulder" in the considered pion spectra (π^- mesons for n^{12}C collisions and π^+ mesons for p^{12}C collisions) indicates that the model underestimates the contribution of D resonances to pion production in the projectile fragmentation region (p^3 1 GeV/c).

Figures 3 and 4 show the normalized experimental data on the transverse momentum distributions of π^- (a) and π^+ (b) mesons in the analysed collisions compared with the calculated theoretical distributions (shown as histograms).

Figures 3 and 4 show that both the experimental and theoretical transverse momentum distributions of the charged pions are smooth and flat for both types of collisions with their tails extending up to $p_t = 1$ GeV/c values. The model overestimates the experimental spectra in the region $p_t < 0.5$ GeV/c and underestimates them at $p_t > 0.5$ GeV/c. In fact, the behaviour of the theoretical transverse momentum distributions reflects the behaviour of the total momentum distributions previously discussed by us, because the emission angle distributions of the charged pions in both the model and the experiment are very close to each other. On the whole, the model qualitatively describes the data on the transverse momentum distributions of the charged pions.

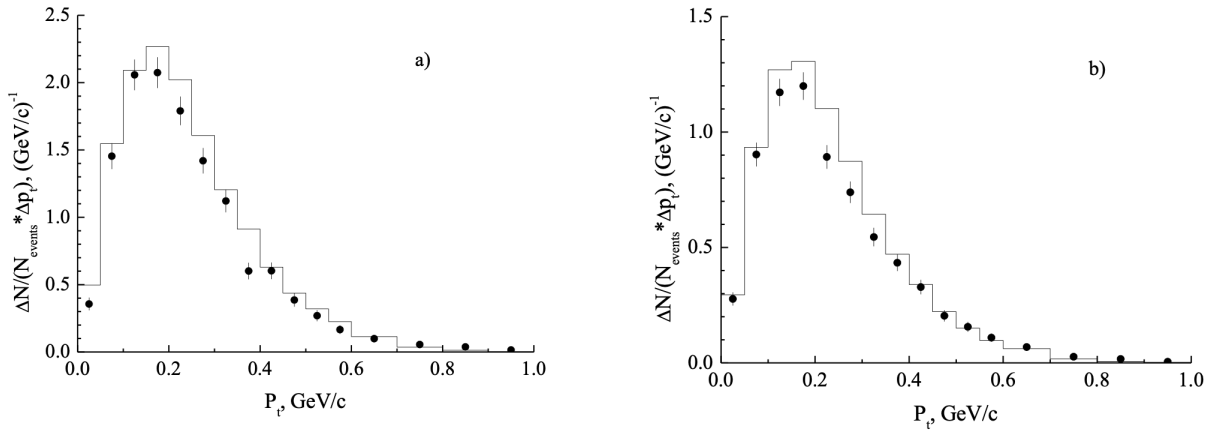

Fig. 3. The normalized transverse momentum distributions of the negative (a) and positive (b) pions in n^{12}C collisions. Histograms—the calculations within the framework of the modified FRITIOF model (Galoyan et al. 2002)

 https://www.doi.org/10.33910/2687-153X-2021-2-3-132-138

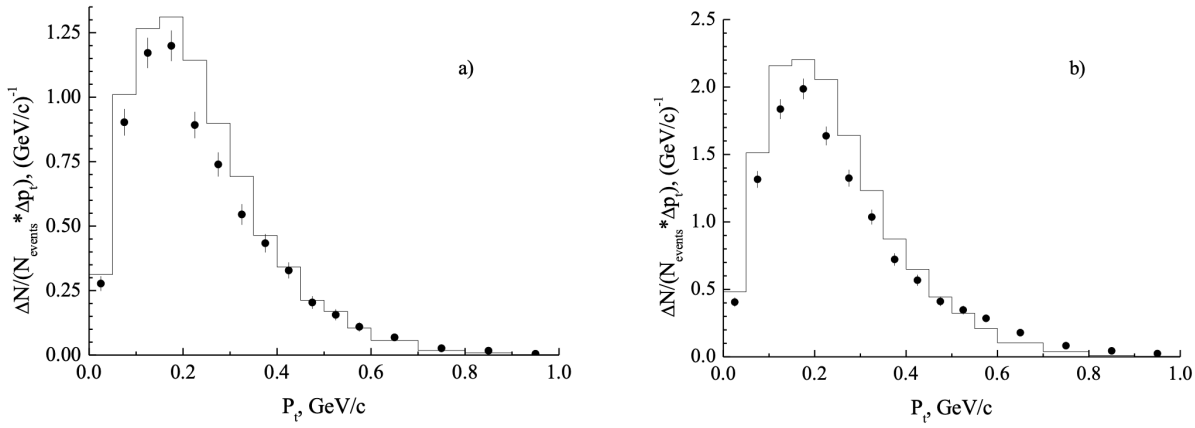

Fig. 4. The normalized transverse momentum distributions of the negative (a) and positive (b) pions in p^{12}C collisions. Histograms—the calculations within the framework of the modified FRITIOF model

Conclusions

We have presented the new experimental data on various properties of the secondary charged pions produced in n^{12}C collisions at 4.2 GeV/c. We have also performed a comparative analysis of the average multiplicities and various kinematic properties of the charged pions produced in n^{12}C and p^{12}C collisions at 4.2 GeV/c. Experimental data were compared systematically with the calculations using the modified FRITIOF model.

It is shown that in n^{12}C (p^{12}C) collisions at 4.2 GeV/c around half of the negative (positive) pions are produced due to inelastic charge exchange reaction (conversion) of the initial neutron (proton) into proton (neutron) and the negative (positive) pion.

The momentum distributions of the negative (positive) pions proved to be more rigid than those of the positive (negative) pions produced in n^{12}C (p^{12}C) collisions. This fact can be related with production of the fast negative (positive) pions due to the inelastic charge exchange reaction (conversion) when the incident neutron transforms into π^- meson and proton, and the decay of the intermediate Δ^0 resonance formed due to excitation of the incident neutron (or when the incident proton transforms into π^+ meson and neutron, and the decay of the intermediate Δ^+ resonance formed due to excitation of the incident proton) in n^{12}C (p^{12}C) collisions, respectively.

It is found that the modified FRITIOF model overestimates the average multiplicities of the charged pions in n^{12}C (p^{12}C) collisions at 4.2 GeV/c compared to the experiment. It is shown that this is due to the fact that the model overestimates the contribution of the intranuclear cascade processes in production of pions in the target fragmentation region compared to the experiment.

It is also found that the model underestimates the multiplicity of the charged pions in the projectile fragmentation region. It is shown that this is due to the fact that the model underestimates the contribution of decays of Δ resonances to the generation of the fast charged pions in the analysed collisions.

Conflict of interest

The authors claim that there is no potential or actual conflict of interest.

References

Azimov, S. A., Gulamov, K. G., Igamberdiev, K. R. et al. (1976) Multiplicity of charged particles in π^--carbon interactions from 4 to 40 GeV/c. *Nuclear Physics B*, 107 (1), 45–64. https://doi.org/10.1016/0550-3213(76)90190-5 (In English)

Bekmirzaev, R. N., Gasparian, A. P., Grishin, V. G. et al. (1984) The multiplicity of the secondary charge particles in inelastic interactions of deuterium and neutrons with tantalum and carbon nuclei at 1.7-GeV/c per nucleon. *Yadernaya fizika*, 40, 1477–1482. (In English)

Botvina, A. S., Chasnikov, I. Ya., Gaitinov, A. S. et al. (1993) Multiplicity of charged particles in inelastic interactions of oxygen nuclei with hydrogen at 3.1 A GeV/C. *Zeitschrift für Physik A Hadrons and Nuclei*, 345 (4), 413–424. https://doi.org/10.1007/BF01282903 (In English)

Galoyan, A. S., Melkumov, G. L., Uzhinskii, V. V. (2002) Analysis of hadron production in nucleus-nucleus interactions up to and out of kinematical limit of free NN-collisions in the frame of FRITIOF model. *Physics of Atomic Nuclei*, 65 (9), 1722–1732. https://www.doi.org/10.1134/1.1508702 (In English)

Olimov, Kh. K., Olimov, K., Lutpullaev, S. L., Yuldashev, B. S. (2007) Comparative analysis of the properties of cumulative π^+ and π^- mesons produced in high-energy proton-nucleus and nucleus-nucleus interactions. *Physics of Atomic Nuclei*, 70 (11), 1974–1976. https://doi.org/10.1134/S1063778807110178 (In English)

Olimov, K., Gulamov, K. G., Lugovoi, V. V. et al. (2007) On the multiplicity distribution of protons in ^{16}O*p* collisions at 3.25 GeV/*c* per Nucleon. *Physics of Atomic Nuclei*, 70 (11), 1977–1979. https://doi.org/10.1134/S106377880711018X (In English)